Structural Chemistry (2024) 35:1719–1742
https://doi.org/10.1007/s11224-024-02294-5

RESEARCH

Crystal structure, molecular docking with SARS-CoV-2 receptors, and potential drug property of tetrahedral Zn(II) complexes

Swah Mohd. Nashre-ul-Islam[1] · Kamala Kanta Borah[1] · Füreya Elif Öztürkkan[2] · Pravin A. Dhakite[3] · Muhammad Asam Raza[4] · Diego M. Gil[5]

Received: 11 January 2024 / Accepted: 6 February 2024 / Published online: 13 April 2024
© The Author(s), under exclusive licence to Springer Science+Business Media, LLC, part of Springer Nature 2024

Abstract

The recent global pandemic by the outbreak of the SARS-CoV-2 virus caused about seven million deaths worldwide. The WHO approved the repurposing of antiviral drugs as the treatment protocol for COVID-19. Yet, it was insufficient to stop the outbreak of COVID-19. By virtue of a broad spectrum of variable oxidation numbers, geometries, tuneable redox, and kinetic and thermodynamic properties, transition metal complexes offer themselves as a viable alternative to the antiviral drugs against SARS-CoV-2. The computational methods in biology and chemistry are a promising starting point in this regard. Here, we present the synthesis, crystal structure, docking study with SARS-CoV-2 receptors, and potential drug property of two tetrahedral Zn(II) complexes, viz. $[Zn(\mu_2\text{-}Bz)_3]_n$ (**1**) and $[Zn(Phen)Cl_2]_2$ (**2**) (Bz = benzoate ion, Phen = *1,10*-phenanthroline). They were synthesized at room temperature and characterized by elemental analyses, FT-IR spectroscopy, thermal analysis (TGA/DTG), powder X-ray diffraction (PXRD), and single crystal X-ray diffraction. Complex **1** is a coordination polymer with unusual triply-bridged triangular secondary building unit (SBU), whereas complex **2** is a novel supramolecular dimer. The crystal structures of **1** and **2** are stabilized by a number of supramolecular interactions, which ultimately lead to a 3D architecture for each of them. Their crystal packing is discussed in details, with inputs from energy calculations, by the analysis of electrostatic potential mapped on the Hirshfeld surface and two-dimensional (2D)-fingerprint plot by CrystalExplorer. A molecular docking study of the synthesized complexes was performed against seven important proteins of SARS-CoV-2. ADMET calculations were used to evaluate their drug potential.

Keywords Zn(II) complexes · Hirshfeld surface analysis · Theoretical study · SARS-CoV-2 · Molecular docking · ADMET calculation

Introduction

Named after its crown-like appearance under an electron microscope, coronaviruses (CoV) caused severe acute respiratory syndrome coronavirus (SARS-CoV) and Middle East respiratory syndrome coronavirus (MERS-CoV) diseases with a very high mortality rate [1]. The World Health Organization (WHO), on March 11, 2020, declared the Coronavirus Disease 2019 (COVID-19) outbreak as a pandemic, caused by another member of the Coronaviridae family: SARS-CoV-2.

SARS-CoV-2 virus genes encode four structural proteins, viz. nucleocapsid (N), membrane (M), spike (S), and envelope (E). These are common features of all coronaviruses [2]. On the other hand, non-structural proteins (NSPs), such as NSP3, also referred to as papain-like protease (PL^{pro}), and NSP5, also referred to as 3-chymotrypsin-like protease

✉ Swah Mohd. Nashre-ul-Islam
smnashreulislam@gmail.com

✉ Diego M. Gil
dmgil@fbqf.unt.edu.ar

1 Department of Chemistry, Mangaldai College, Assam-784125 Guwahati, India

2 Department of Chemical Engineering, Kafkas University, Kars, Turkey

3 Department of Chemistry, S. N. Mor Arts, Com. and Smt. G. D. Saraf Science College, Tumsar Maharashtra 441912, India

4 Department of Chemistry, Hafiz Hayat Campus, University of Gujrat, Gujrat, Pakistan

5 INBIOFAL (CONICET–UNT) Instituto de Química Orgánica, Facultad de Bioquímica, Química y Farmacia, Universidad Nacional de Tucumán, Ayacucho 471, T40 0 0INI San Miguel de Tucumán, Argentina

(3-CL^{pro}) or main protease (M^{pro}) and RNA-dependent RNA polymerase (RdRp), are encoded by the open reading frame (ORF) region [3, 4].

In the course of viral infection of a cell, the receptor binding domain of SARS-CoV-2 spike protein first, using spike glycoproteins (S-glycoproteins), binds at the cell surface protein angiotensin-converting enzyme II (ACE-2). ACE-2, a Zn-dependent metalloenzyme, thus serves as a cellular entry receptor for SARS-CoV-2. As a result, inhibition of the interaction of spike proteins with ACE-2 could potentially block the viral entry into the host cells. Binding to ACE-2 receptors causes conformational changes in the S-glycoprotein. This allows cleavage of the S-glycoprotein by the host cell trans-membrane protease-serine 2. The spike protein is primed, and the virus is transported into the host cell cytoplasm through a mechanism called endocytosis [5–8].

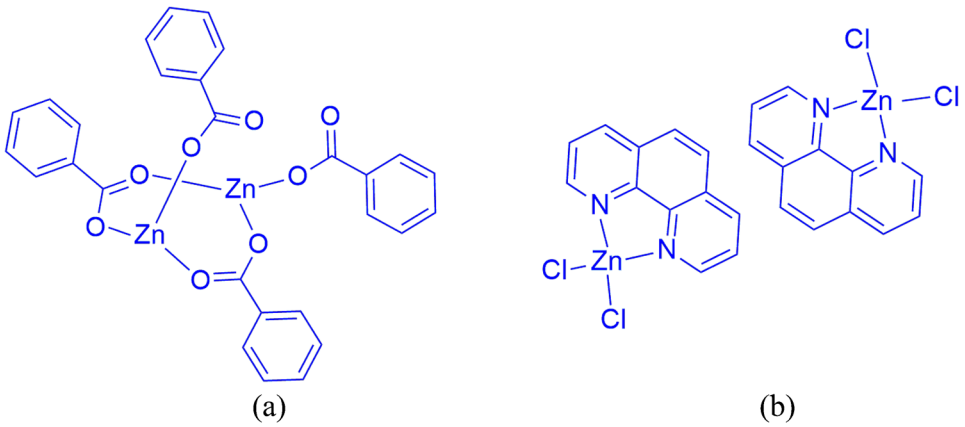
Upon translation of the open reading frames, ORF1a and ORF1b from the genomic RNA, two polyproteins viz. pp1a and pp1ab are generated with co-translational release of sixteen non-structural proteins (NSPs). Among these, PL^{pro} and M^{pro} are responsible for the proteolytic processing of the majority of the polyprotein cleavage sites. The cleavage of SARS-CoV-2 polyproteins by M^{pro} is facilitated by Cys145 and His41, which form a catalytic dyad [9, 10]. The viral life cycle, thus, can be disrupted by the interference with the activity of these proteases. This provides additional targets for therapeutic intervention [11–13]. Also, the fact that M^{pro} is highly conserved renders it an attractive therapeutic target for SARS-CoV-2 inhibition [14].

Health organizations have proposed various methods for the treatment of COVID-19 using the available drugs. For example, repurposing of various antimalarial/antiviral drugs such as chloroquine, tenofovir, galidesivir, sofosbuvir, remdesivir, and ribavirin was recommended for its treatment. These drugs inhibited the RNA-dependent RNA polymerase (RdRp) complex of SARS-CoV-2. The molecular docking studies were performed to determine the binding energy between RdRp and the above drugs, which revealed values of −5.1, −6.9, −7.0, −7.5, −7.6, and −7.8 kcal/mol, respectively [15]. In a large number of reports, treatment of COVID-19 using organic molecules as medicines has been suggested [16]. As an alternative, however, inorganic complexes, whose biological activities are well established in the literature, have also been explored [17–22]. Complexation with metal ions alters the pharmacological and therapeutic effects of the coordinating ligands. This opens new opportunities for the design of useful metal-based drugs in medicinal chemistry [23]. The potential of metal complexes as antiviral agents, including that for COVID-19, has recently been reported by various groups [24–26]. Their binding mechanism and sensitivities towards SARS-CoV-2 receptors have been studied by molecular docking study. For example, the docking study of novel Cu(II) and Ni(II) Schiff base coordination complexes with M^{pro} of the SARS-CoV-2 virus showed binding energy values of −8.5 and −11.5 kcal/mol, respectively [27]. A novel Mn(II) complex with another Schiff base showed a strong binding affinity with the unliganded active site of SARS-CoV-2 M^{pro} proteins, as demonstrated by molecular docking with a high binding energy value of −10.10 kcal/mol [28]. Similarly, novel Schiff base metal complexes were explored as dual inhibitors for M^{pro} and non-structural protein 16 (NSP16) of SARS-CoV-2, where Ni(II) and Zn(II) complexes showed excellent binding energies [29]. Molecular docking study of mononuclear and dinuclear Cu(II) α-aminophosphonate complexes was also performed against two SARS-CoV-2 coronavirus protein targets, which showed that the mononuclear species bound more strongly with the targets than the dinuclear ones [30].

From the 1970s to the present, the use of Zn has been studied against viruses, where Zn was found to affect protein synthesis and processing, viral replication, membrane fusion, and RNA polymerase activity [31, 32]. As for SARS-CoV-2, RNA-dependent RNA-polymerase (RdRp) and M^{pro} play a key role in its replication. Zinc has strong immunogenic properties and is found to bind to a number of proteins, thereby modulating their activities [33]. The success of hydroxychloroquine and chloroquine therapy for COVID-19 treatment also involves their roles as an ionophore of Zn(II), whereby more Zn(II) ions are brought into the cells. Due to its direct inhibitory effect on the SARS-CoV-2 replicative cycle, Zn(II) can be a promising and potential candidate for COVID-19 treatment [34].

We have synthesized and reported a number of novel coordination complexes with interesting supramolecular architectures, stabilized by various unusual non-covalent interactions [35–37]. Recently, we have reported a novel Zn(II) coordination polymer involving 2-aminopyridine and bridging *o*-phthalato ligands, which is mainly stabilized by C−H···H−C interactions [38]. Its docking study with six important SARS-CoV-2 proteins revealed good docking scores. In continuation of our effort to synthesize novel coordination complexes with interesting supramolecular architectures and explore them as therapeutic agents against SARS-CoV-2, we, herein, present the synthesis, crystal structure, Hirshfeld surface analysis, and theoretical study of two tetrahedral coordination complexes of Zn(II) with bridging benzoato (Bz) and *1,10*-phenanthroline (Phen) ligands, viz. $[Zn_2(\mu_2\text{-}Bz)_3]_n$ (**1**) and $[Zn(Phen)Cl_2]_2$ (**2**) (Scheme 1). Complex **1** is a coordination polymer involving unusual triply-bridged triangular secondary building unit (SBU), whereas **2** is novel a supramolecular dimer, extensively stabilized by π···π interactions. The pharmacokinetic and toxicokinetic features support these complexes as good drug candidates. Their docking study with various important

Scheme 1 Complexes **1** (**a**) and **2** (**b**)



proteins of SARS-CoV-2 revealed good docking scores, particularly for **1**. The therapeutic potentials of **1** and **2** were evaluated by ADMET calculations.

Experimental

Materials and methods

All reagents viz. zinc(II) chloride, $ZnCl_2$, benzoic acid, *1,10*-phenanthroline and sodium hydroxide were obtained from Sigma Aldrich and Merk (India) Ltd. All chemicals were of analytical grade. They were used as received without further purification. The reaction was carried out in the deionized water medium. Elemental (C, H, and N) analyses were carried out in a Perkin Elmer 2400 Series II CHNS/O analyzer. KBr phase FT-IR spectrum was recorded in a Shimadzu FTIR-8400S spectrophotometer in the mid-IR region (4000 to 600 cm^{-1}). Thermogravimetric studies were carried out using a Mettler Toledo TGA/DSC1 STAR^e system at a heating rate of 10 °C min^{-1} under a flow of N_2 gas. The powder X-ray diffraction data were obtained using a XPERT-PRO X-ray powder diffractometer.

Synthesis of the complexes

Synthesis of $[Zn_2(\mu_2\text{-}Bz)_3]_n$ (1)

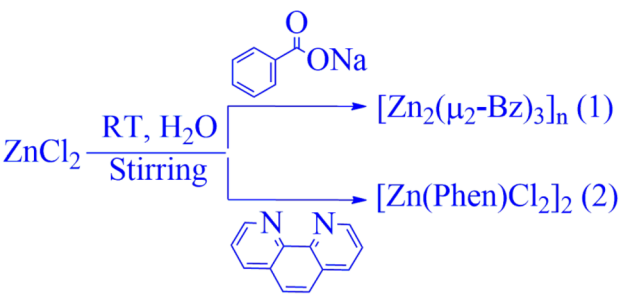
Benzoic acid (0.122 g, 1.0 mmol) was dissolved in 15 ml of distilled water in a round-bottom flask containing NaOH (0.040 g, 1.0 mmol). An aqueous solution of $ZnCl_2$ (0.136 g, 1.0 mmol) was added to the above solution. The colorless solution was stirred at room temperature for about 4 h (Scheme 2). The solution was filtered and the filtrate freezed. Colorless block-shaped crystals of **1** suitable for X-ray analysis were obtained from the filtrate after 2 weeks with a yield of 72.3% based on $ZnCl_2$. The crystals were filtered off, washed well with distilled water and dried in air. Elemental analysis (%): Calcd for $Zn_2C_{28}H_{20}O_8$: C, 53.45; H, 3.20. Found: C, 53.41; H, 3.16. IR (KBr pellet, cm^{-1}): 1637 (m), 1598 (m), 1532 (s), 1404 (s), 1169 (w), 1073 (w), 1028 (w), 810 (m), 714 (s), 682 (sh).

Synthesis of $[Zn(Phen)Cl_2]_2$ (2)

1,10-Phenanthroline (0.180 g, 1 mmol) was added to an aqueous solution of $ZnCl_2$ (0.136 g, 1 mmol) in a round-bottom flask. The colorless solution was stirred for about 5 h (Scheme 2). The solution was filtered and the filtrate freezed. Colorless block-shaped crystals of **2** suitable for X-ray analysis were obtained from the filtrate after 1 week with a yield of 69.5% based on $ZnCl_2$. The crystals were filtered off, washed well several times with distilled water and dried in air. Elemental analysis (%): Calcd for $ZnC_{12}H_8Cl_2N_2$: C, 45.54; N, 8.85; H, 2.55. Found: C, 45.51; N, 8.82; H, 2.52. IR (KBr pellet, cm^{-1}): 1598 (m), 1550 (s), 1411 (s), 1355 (s), 1220 (w), 1143 (w), 1104 (w), 1047 (w), 906 (w), 844 (s), 778 (w), 722 (s), 650 (w).

X-ray crystallographic study

Molecular and crystal structures of **1** and **2** were determined by single crystal X-ray diffraction technique. Their intensity data was collected on a Bruker SMART APEX IICCD



Scheme 2 Syntheses of **1** and **2**

equipped with a graphite monochromatized Mo-Kα radiation ($\lambda = 0.71073$ Å) at 296 K. SAINT [39] was used for data integration. Intensities for absorption were corrected using SADABS [40]. The structures were solved by the direct method in the monoclinic $P2_1/c$ (**1**) and P_n (**2**) space groups with SHELXS-97 [41] and refined on F^2 using full matrix least squares techniques in the anisotropic approach for non-hydrogen atoms via WinGX [42]. The aromatic hydrogen atoms were placed at calculated positions and refined by standard procedures of SHELXL-97. The structural illustrations have been drawn using Diamond 3.0 [43]. Data collection and refinement parameters for **1** and **2** are summarized in Table 1.

Hirshfeld surface calculations

Hirshfeld surfaces provide a three-dimensional picture for exploring the main packing modes and close contacts that are responsible for the crystal packing of organic and inorganic compounds, including coordination compounds [44–47]. The molecular Hirshfeld surfaces (HSs) and their associated two-dimensional fingerprint plots (FPs) were generated for complexes **1** and **2**, based on their crystallographic information file (.cif), by using the Crystal Explorer 21.5 program [48]. The 3D HSs were mapped over d_{norm} (normalized contact distance), *shape index*, and *curvedness* properties. For each point on the isosurface, two distances are defined as d_e (the distance from the point to the nearest nucleus external to the surface) and d_i (the distance to the nearest nucleus internal to the surface). The normalized contact distance (d_{norm}) based on both d_e and d_i and the van der Waals (vdW) radii of atoms enable the identification of the regions that are involved in the main intermolecular interactions. The distances equal to the sum of vdW atomic radii are represented as white regions, and the contacts with distances shorter and longer than the sum of vdW atomic radii are shown as red and blue colors, respectively. Moreover, two further colored properties based on the local curvature

Table 1 Crystal data and structure refinement of **1** and **2**

Crystal data	$[Zn_2(\mu_2\text{-}Bz)_3]_n$ (**1**)	$[Zn(Phen)Cl_2]_2$ (**2**)
CCDC number	2210554	2210555
Empirical formula	$Zn_2C_{28}H_{20}O_8$	$ZnC_{12}H_8Cl_2N_2$
Formula weight	615.18	316.47
Temperature (K)	293(2)	296(2)
Wavelength (Å)	0.71073	0.71073
Crystal system	Monoclinic	Monoclinic
Space group	$P2_1/c$	P_n
a (Å)	10.817(5)	8.009(4)
b (Å)	12.629(5)	15.711(8)
c (Å)	18.838(5)	9.762(5)
α (°)	90.000(5)	90
β(°)	100.770(5)	100.312(11)
γ(°)	90.000(5)	90
Volume (Å^3)	2528.1(17)	1204.4(11)
Z	4	4
Calculated density (Mgm^{-3})	1.616	1.745
Absorption coefficient (mm^{-1})	1.948	2.457
F(000)	1248	632
Crystal size (mm^3)	28 × 20 × 15	25 × 19 × 16
θ range for data collection (°)	1.92 to 28.95	1.30 to 28.73
Index ranges	$-14 \le h \le 14$, $-17 \le k \le 17$, $-25 \le l \le 25$	$-10 \le h \le 10$, $-21 \le k \le 21$, $-13 \le l \le 13$
Reflections collected	92,366	49,343
Unique data [R_{int}]	6627 [0.1377]	6190 [0.0508]
Refinement method	Full-matrix least-squares on F^2	Full-matrix least-squares on F^2
Data / restraints / parameters	667 / 0 / 343	6190 / 2 / 309
Goodness-of-fit on F^2	1.083	1.011
Final R indices[$I > 2\sigma(I)$] $R1$/ $wR2$	$R1 = 0.0850$, $wR2 = 0.1452$	$R1 = 0.0302$, $wR2 = 0.0698$
R indices(all data) $R1$/ $wR2$	$R1 = 0.0757$, $wR2 = 0.1567$	$R1 = 0.0457$, $wR2 = 0.0791$
Largest diff. peak and hole (e.Å^{-3})	1.370 and −1.452	0.340 and −0.584

of the surface such as shape index and curvedness were also shown. The combination of d_e and d_i in the form of a 2D fingerprint plot provides a detailed summary of the intermolecular contacts in the crystal lattice [49]. The 2D fingerprint plots were generated by using the translated (1.0–2.8 Å) range, and reciprocal contacts were also included.

Theoretical methods

The calculations of the non-covalent interactions have been performed using the Gaussian 09, Rev D01 program [50] and the B3LYP-D3/def2-TZVP level of theory [51, 52]. The intermolecular interactions observed in the solid state have been evaluated by using the crystallographic coordinates from the X-ray crystal structure. The dimerization energies were estimated by calculating the difference between the isolated monomers and their assembly. Bader's "Atoms in Molecules" theory (QTAIM) [53] has been used to study the intermolecular interactions by means of the Multiwfn software [54]. The molecular electrostatic potential (MEP) surfaces have been computed by using the Gaussian 09, Rev D01 program. The NCI isosurfaces plots were used to characterize the non-covalent interactions [55]. The color scale is red-yellow-green-blue scale with red and blue-green isosurfaces for repulsive and attractive interactions, respectively. The NCI plot isosurfaces have been computed by means of the Multiwfn program [54] and represented using VMD software [56].

Prediction of pharmacokinetic and toxicological properties

The characteristics of a drug that express its pharmacokinetics in the human body are referred to as absorption, distribution, metabolism, excretion, and toxicity (ADMET). Lipinski's rule of 5 states [57] that when there are no more than five hydrogen bond donors and acceptors, no molecular weight more than 500 g/mol, and an octanol/water partition coefficient greater than five, absorption or permeability is more likely. In this investigation, we used the SwissADME online database [58] to assess the absorption, distribution, metabolism, and excretion characteristics of two synthesized complexes and screened them using the Lipinski 5 rule. We further investigated the complexes' toxicity risk assessment properties using the ProTOX-II online database [59].

In silico assay

Autodock Vina [60] was used to compute the binding affinity between complexes **1** and **2** with the proteins of SARS-CoV-2. The proteins of SARS-CoV-2 were downloaded from the RCSB Protein Data Bank (https://www.rcsb.org). (spike protein of first variant (PDB Code: 6M0J) [61], spike protein of Omicron variant (PDB Code: 7T9J) [62], main protease (PDB Code: 7BQY) [63], papain-like protease (PDB Code: 6W9C) [64], NSP12-NSP7-NSP8 complex (PDB Code: 7BV2) [65], NSP15 Endoribonuclease (PDB Code: 6WXC) [66], NSP16-NSP10 heterodimer (PDB Code: 6WKQ) [67], transmembrane protease (PDB Code: 7MEQ) [68]. Water molecules from the protein structure were removed, and polar hydrogens and Kollman charges were added. The ligand's torsions were allowed to rotate, and the determined residues were tested. The ligands were docked blindly to see where they would preferentially bind. The amino acids in the active site of all proteins were determined using the BIOVA Discovery Studio Visualizer 2021 [69]. The Lamarckian Genetic Algorithm was utilized as a docking engine, with all docking settings set to default. The visualization studies were performed using the BIOVA Discovery Studio Visualizer 2021.

Results and discussion

Synthesis and general aspects

The polymer $[Zn_2(\mu_2\text{-}Bz)_3]_n$ (**1**) has been isolated in high yield by reacting one equivalent of zinc chloride, $ZnCl_2$ with one equivalent of sodium benzoate in water. The μ^2:$\eta^1\eta^1$ bridging ability of the benzoato ligand imparts polymeric nature to **1**. It was previously reported [70] in a different way with different starting materials. Here, we have synthesized it in a rather simple way. Similarly, the supramolecular dimer $[Zn(Phen)Cl_2]_2$ (**2**) has been isolated in high yield by reacting one equivalent of zinc chloride with one equivalent of *1,10*-phenanthroline in water. Its asymmetric unit consists of two same $[Zn(Phen)Cl_2]$ monomeric units, albeit the Zn−N and Zn−Cl distances are different in them. The complexes are slightly soluble in water, and their solubility in common organic solvents is also low. They show a room temperature μ_{eff} value of 0.00 BM each, thereby confirming the absence of unpaired electrons in the respective metal center.

FT-IR spectra

FT-IR spectra of **1** and **2** (KBr pellets) were recorded in the region 4000–600 cm^{-1} (Fig. 1). The observed bands are tentatively assigned based on earlier literature reports [71, 72]. The absence of absorption bands in the range 1750–1670 cm^{-1} indicates that the $–COO^-$ groups in **1** remain completely de-protonated. In the region expected for the asymmetric, ν_a (COO^-) absorption, polymer **1** exhibits one single sharp and strong band at 1532 cm^{-1}, implying that the structure has only one type of carboxylate bridging in it. The band at 1404 cm^{-1} of the carboxylate, $–COO^-$ group

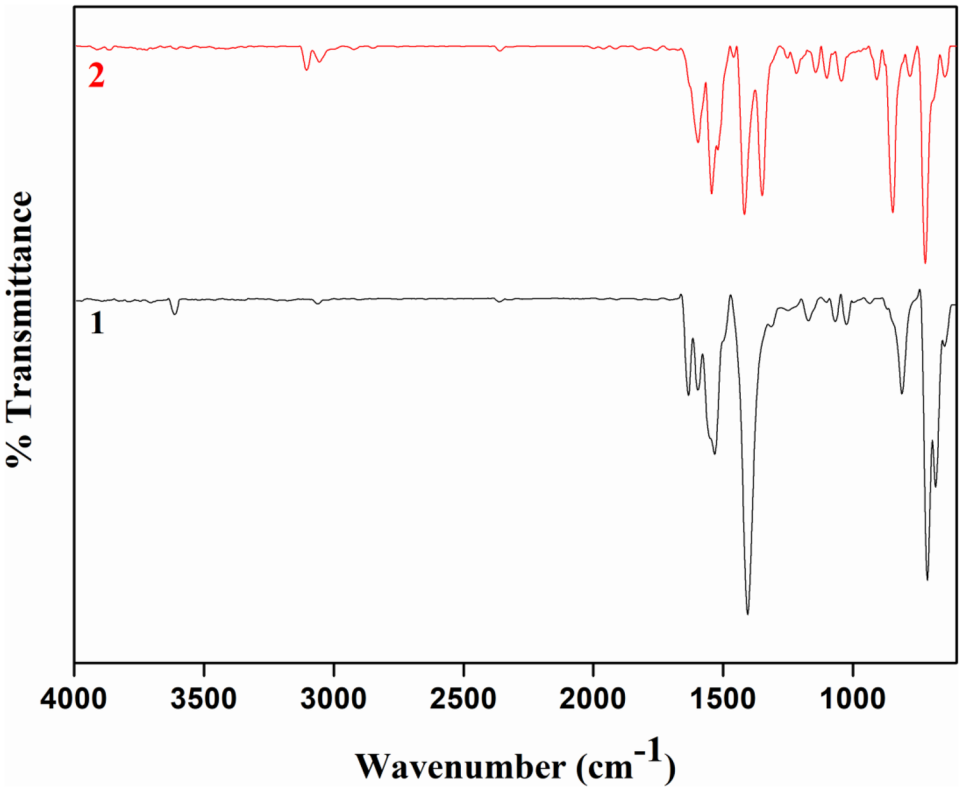


Fig. 1 FT-IR spectra of **1** and **2**

corresponds to its symmetric (ν_s) stretching vibrations. Their difference [$\Delta = \nu_a - \nu_s = 128$ cm^{-1}] suggests the *syn-syn* bidentate bridging mode (μ_2:η^1:η^1) of the exogeneous benzoate group to the metal center. On the other hand, the $\nu_{C=N}$ of *1,10*-phenanthroline ligand at 1561 cm^{-1} shifts to 1550 cm^{-1} in **2**. Similarly, the δ_{C-H} at 854 and 736 cm^{-1} of *1,10*-phenanthroline ligand shift to 844 and 722 cm^{-1} in this complex. This reveals the coordination of the two nitrogen atoms of *1,10*-phenanthroline ligand to the Zn(II) ions in **2** [73]. These observations are in good agreement with the structures of **1** and **2** as determined by single-crystal XRD and elemental analyses.

Powder X-ray diffraction

The phase purity of the synthesized complexes **1** and **2** were studied by powder X-ray diffraction (PXRD) experiment. As shown in Fig. 2, their experimental patterns are in good agreement with the simulated ones obtained from the corresponding single-crystal X-ray diffraction data, suggesting that the synthesized crystals of **1** and **2** are true representatives of their bulk material. The observed differences in intensity between the simulated and experimental patterns may be due to the preferential orientations of the crystalline powders.

Crystal structure of the complexes

Crystal structure of $[Zn_2(\mu_2\text{-}Bz)_3]_n$ (1)

The details of single crystal XRD and structure refinement data of polymer **1** are presented in Table 1. It crystallizes in the monoclinic space group $P2_1/c$. The polymeric unit of **1** is shown in Fig. 3, together with the atomic numbering scheme (Fig. 3a). The crystal structure of the polymer **1** contains a basic dimeric unit $[Zn_2(\mu_2\text{-}Bz)_3]$ with a Zn···Zn distance of 3.25 Å. These are linked together by another bridging benzoate anion in the *syn, syn*-η^1:η^1:μ_2 coordination mode, thereby forming a metal-binding site of O_4 type around each Zn center. Each Zn(II) ion in **1**, thus, possesses a distorted tetrahedral coordination environment built by the benzoate oxygens (O2, O3, O6, O7 for Zn1 and O1, O4, O5, O8 for Zn2). The coordination angles about the Zn centers are in the range 98.40(12)−113.92(13)° except for O3−Zn1−O6 of 121.88 (12)°. The extent of distortion of the tetrahedron around the Zn(II) ions can be indicated by the Houser [74] parameter, τ_4. For **1**, the value of τ_4 is 0.86 for Zn1 and 0.94 for Zn2 (for an ideal tetrahedron, $\tau_4 = 1$). The distortion at each Zn(II) center in **1** is partly due to the spatial orientation of the bridging benzoato ligands. The selected bond lengths (Å) and bond angles (°) of **1** are presented in Table 2. These values are comparable with those in similar compounds in literature [75, 76].

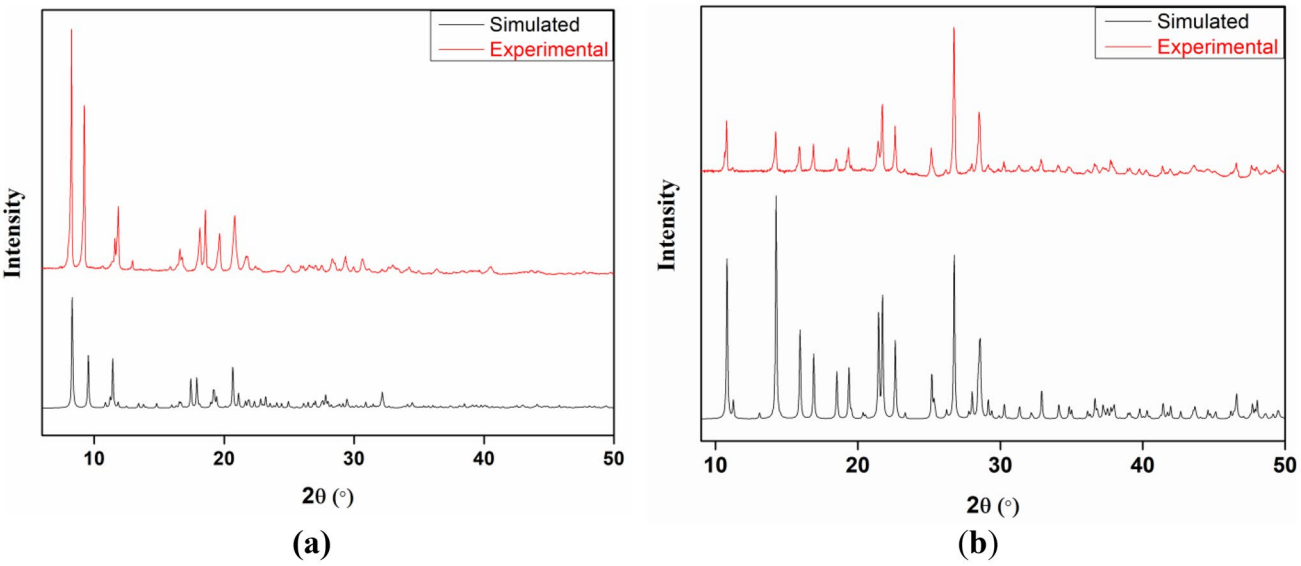


Fig. 2 Simulated and experimental PXRD patterns of **1** (**a**) and **2** (**b**)

The $Zn_2(CO_2)_3$ unit (Fig. 3c) in **1** merits some discussion. The common SBUs are generally composed of four identical carboxyl groups [77], with paddle-wheel geometry. The above unit in **1** is unique in that it is a triply-bridged SBU with a triangular shape. The planes through the carboxylate groups O1−C1−O2, O3−C8−O4, and O5−C15−O6 of the bridging benzoato ligands make dihedral angles of 3.04(6), 5.95(6), and 22.42(2)° with the respective aromatic rings. The interlinking of the dimeric units, $[Zn_2(\mu_2\text{-}Bz)_3]$ of **1** by the bridging benzoate anion results in a linear 1D polymeric chain that extends along the crystallographic *b*-direction.

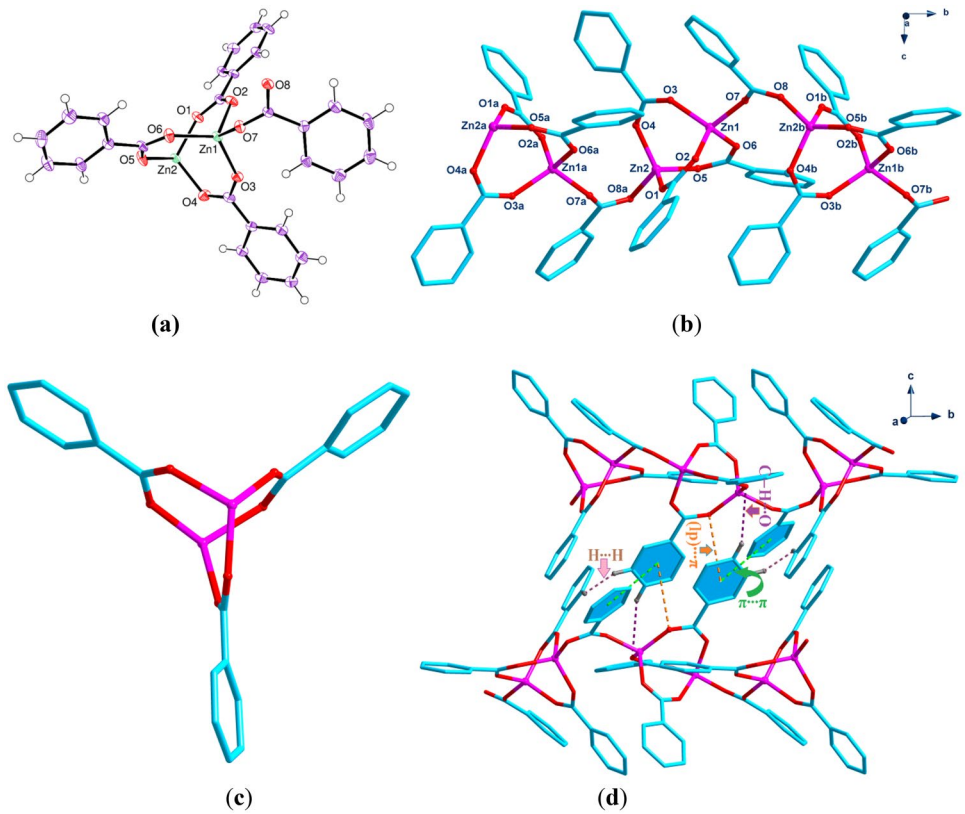


Fig. 3 **a** ORTEP diagram of **1** with the partial atomic labeling scheme, showing 50% probability ellipsoids. **b** View of the coordination environment of Zn atoms in **1**. Symmetry codes: a. 1 − x, −0.5 + y, 0.5 − z; b. 1 − x, 0.5 + y, 0.5 − z. **c** Unusual triply-bridged triangular secondary building unit (SBU) of **1**. **d** Interconnection of polymeric chains of **1** in the *bc*-plane. Interactions between adjacent polymeric chains are only shown. Irrelevant hydrogen atoms are omitted for clarity

Table 2 Selected bond lengths (Å) and bond angles (°) of **1**

Bond	d (Å)	Angle	θ(°)
Zn1−O2	1.942 (3)	O2−Zn1−O3	102.89 (12)
Zn1−O3	1.951 (3)	O2−Zn1−O6	116.77 (13)
Zn1−O6	1.936 (3)	O2−Zn1−O7	105.80 (12)
Zn1−O7	1.937 (3)	O3−Zn1−O6	121.88(12)
Zn2−O1	1.946 (4)	O3−Zn1−O7	109.69 (11)
Zn2−O4	1.940 (3)	O6−Zn1−O7	98.76 (13)
Zn2−O5	1.954 (3)	O1−Zn2−O4	113.92 (13)
Zn2−O8	1.942 (3)	O1−Zn2−O5	113.46 (13)
		O1−Zn2−O8	111.79 (13)
		O4−Zn2−O5	109.69 (12)
		O4−Zn2−O8	108.44 (13)
		O5−Zn2−O8	98.40 (12)

These chains are interconnected in two perpendicular directions. Along the *bc*-plane, these are connected through antiparallel π···π stacking interactions between the phenyl rings, C9−C14 and C23−C28 of the coordinated benzoato ligands from adjacent chains. This is in accordance with their positive and negative MEP values, respectively (*vide infra*). It is interesting to note that there occurs no π···π interaction between the C9−C14 phenyl rings of benzoate ligands from adjacent chains, although their distance of separation is favorable for the same. This architecture, with the shortest inter-chain Zn···Zn distance of 9.22 Å, is stabilized by C−H···O, C−H···H−C, and lone-pair (lp) O···π interactions. The O6 atom of the bridging carboxylato ligand in one chain acts as a hydrogen-bond acceptor for the C12−H12 moiety of another bridging carboxylato phenyl ring in the adjacent chain to form weak C12−H12···O6 hydrogen bond with a donor-acceptor distance of 3.73 Å. Similarly, the C7−H7 moiety of the bridging benzoato ligand in one polymeric chain is involved in C−H···H−C interaction with the C13−H13 moiety of the same ligand from a neighboring chain.

Additional reinforcement to this architecture is provided by the lone-pair (lp)···π interaction involving the O3-atom of the coordinated carboxylato ligand. In the layered architecture of **1** in the *bc*-plane, an interesting contact between C=O moiety of the coordinated carboxylato ligand from one polymeric chain and the π-system of the same ligand from an adjacent chain is observed, where the coordinated O3 atom is oriented towards the π−face of the phenyl ring. The separation distance between this O3-atom and the centroid of the concerned phenyl ring is 3.67 Å. Here, the carbonyl oxygen, O3 approaches the π-face with an angle of 87.1°, suggesting a strong lone-pair···π interaction. Such lone-pair···π interactions are characterized by two important parameters: the distance, D (between the carbonyl oxygen atom and the ring centroid, C_g), and the angular distribution (deviation of α from 120°, where α is the angle between C=O···C_g). For **1**, these values are 3.67 Å and 33.0°, respectively. These values are within the acceptable range for favorable lone-pair···π interactions found in the CSD [78]. Not surprisingly, **1** thus provides an example of carbonyl (lp)···π interaction involving an aromatic ring, where the π-system is electron poor (*vide infra*).

In the *ab*-plane, however, the polymeric chains of **1** with the shortest inter-chain distance of 9.89 Å are interconnected by C−H···π interactions to give a layered architecture (Fig. 4a). This involves the H27 atom from the phenyl ring (C23−C28) of coordinated benzoato ligand from one chain and the centroid (C_g) of another phenyl ring (C9−C14) from a neighboring chain [d(H27···C_g) = 3.49 Å]. The formation of such layered structures of **1** in two perpendicular directions ultimately gives rise to a 3D architecture of **1** along *b*-direction (Fig. 4b).

Crystal structure of $[Zn(phen)Cl_2]_2$ (2)

The details of single crystal XRD and structure refinement data of compound **2** are presented in Table 1. It crystallizes in the monoclinic space group P_n. In the asymmetric

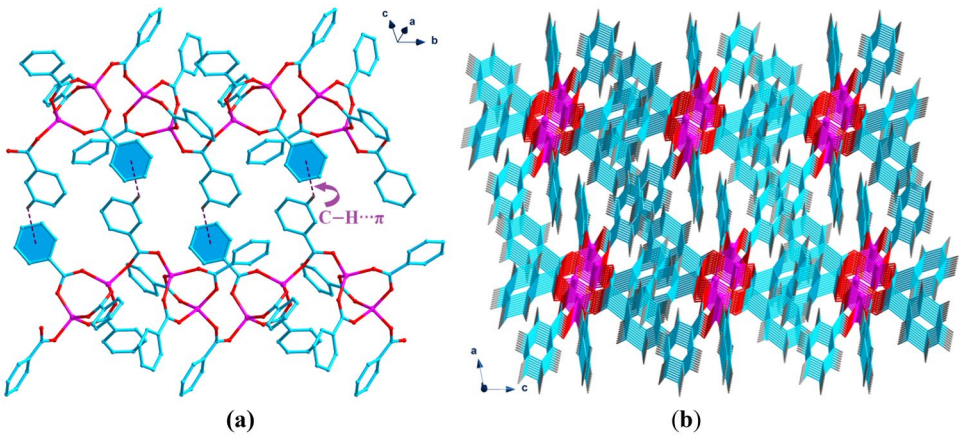


Fig. 4 **a** Interconnection of polymeric chains of **1** in the *ab*-plane through C−H···H−C contacts. Interactions between adjacent polymeric chains are only shown. Irrelevant hydrogen atoms are omitted for clarity. **b** View of 3D architecture of **1** along *b*-direction

unit of **2**, there are two similar (but not same!) neutral units, each consisting of one zinc(II) ion, one chelating *1,10*-phenanthroline ligand, and two chloride ions as terminal ligands (Fig. 5a). Each Zn(II) is four coordinated in a tetrahedral geometry by two nitrogen atoms from *1,10*-phenanthroline ligand and two chloride ions. The coordination angles about the Zn centers are in the range 80.29 (28)−125.28 (18)° except for N2−Zn1−Cl1 of 125.28 (18)°. The extent of distortion from the regular tetrahedral geometry around the Zn(II) ions is indicated by the Houser [74] parameter, τ_4. For **2**, this value is 0.85 for Zn1 and 0.84 for Zn2. The selected bond lengths (Å) and bond angles (°) of **2** are presented in Table 3.

From a structural viewpoint, complex **2**, which is a supramolecular dimer, is rather interesting. The two monomeric units have the same composition, yet the Zn−N and Zn−Cl distances therein are different. The monomeric counterpart of **2**, viz. [Zn(phen)Cl_2] has already been synthesized, albeit in a different way [79, 80]. The Zn−N and Zn−Cl distances and important bond-angles in **2** are similar to those in the previously synthesized monomeric counterparts.

The solid state structure of complex **2** shows a combination of π···π, C−H···Cl, C−H···H−C, and lone-pair (Cl)···π interactions. First of all, its supramolecular dimer is stabilized by extensive π···π interactions with the pyridyl ring of *1,10*-phenanthroline ligand from one monomeric unit overlapping with the pyridyl and phenyl rings of the same ligand from the second monomeric unit at centroid-to-centroid separations of 3.67, 3.68 and 3.80 Å (Fig. 5b). The dimer is further reinforced by intramolecular self-complementary C−H···Cl hydrogen bonds with H···Cl distances of 2.76 and 2.84 Å.

Along *a*-direction, neighboring molecules of **2** self-assemble through π···π interactions, involving the pyridyl ring of one molecule and the phenyl ring of the other (Fig. 6a). Although the interacting rings are the same for the two interactions, their distances are, however, different (3.80 and 3.81 Å). This self-assembly of the molecules of **2** through π···π interactions gives rise to a linear chain of **2** along *a*-direction. In a similar manner of **1**, these chains of **2** interconnect themselves in two perpendicular directions through C−H···Cl, C−H···H−C, and lone-pair (Cl)···π interactions.

Table 3 Selected bond lengths (Å) and bond angles (°) of **2**

Bond	d (Å)	Angle	θ(°)
Zn1−N2	2.073 (7)	N1−Zn1−N2	81.98 (25)
Zn1−N3	2.085 (7)	N1−Zn1−Cl1	108.30 (17)
Zn1−Cl1	2.215 (3)	N1−Zn1−Cl2	106.99 (18)
Zn1−Cl2	2.211 (3)	N2−Zn1−Cl1	125.28 (18)
Zn2−N3	2.072 (8)	N2−Zn1−Cl2	106.99 (17)
Zn2−N4	2.054 (7)	Cl1−Zn1−Cl2	114.58 (92)
Zn2−Cl3	2.220 (3)	N3−Zn2−N4	80.29 (28)
Zn2−Cl4	2.197 (3)	N3−Zn2−Cl3	108.10 (17)
		N3−Zn2−Cl4	124.15 (18)
		N4−Zn2−Cl3	115.94 (18)
		N3−Zn2−Cl4	108.76 (19)
		Cl3−Zn2−Cl4	115.12 (11)

In the *ab*-plane, the Cl3 atoms in different dimers act as H-bond acceptors for C3−H3 and C23−H23 moieties of *1,10*-phenanthroline ligand from neighboring chains with donor-acceptor distances of 3.69 and 3.55 Å, respectively (Fig. 6b). This gives rise to a layered architecture of **2** in the *ab*-plane, which is further stabilized by another C−H···Cl interaction involving the Cl2 ligand (Table 4). In the *ac*-plane as well, these 1D chains of **2** get interconnected through two types of C−H···Cl interactions involving both the monomeric units (Fig. 6c). One monomeric unit is connected with an adjacent 1D chain through C2−H2···Cl2 interaction with H2···Cl2 distance of 2.93 Å (Table 4). The other monomeric unit gets connected with another adjacent 1D chain, in a direction opposite to the former, through C3−H3···Cl23 interaction [2.83 Å]. This gives rise to a layered structure of **2** in this plane. In this structure, the chlorine atoms Cl1, Cl2, Cl3, and Cl4 in one chain are located above the plane of the *1,10*-phenanthroline pyridine rings in the neighboring chain. Thus, the layered structure of **2** in the *ac*-plane is stabilized by extensive lone-pair (Cl)···π interactions. This is further stabilized by C−H···H−C interactions. The C6−H6 and C20−H20 moieties of *1,10*-phenanthroline

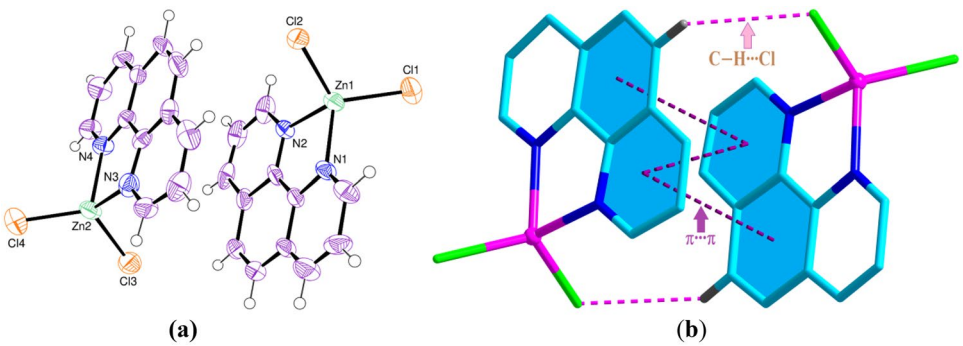


Fig. 5 **a** ORTEP diagram of **2** with the partial atomic labeling scheme, showing 50% probability ellipsoids. **b** π···π and self-complimentary C−H···Cl interactions-stabilized supramolecular dimer of **2**

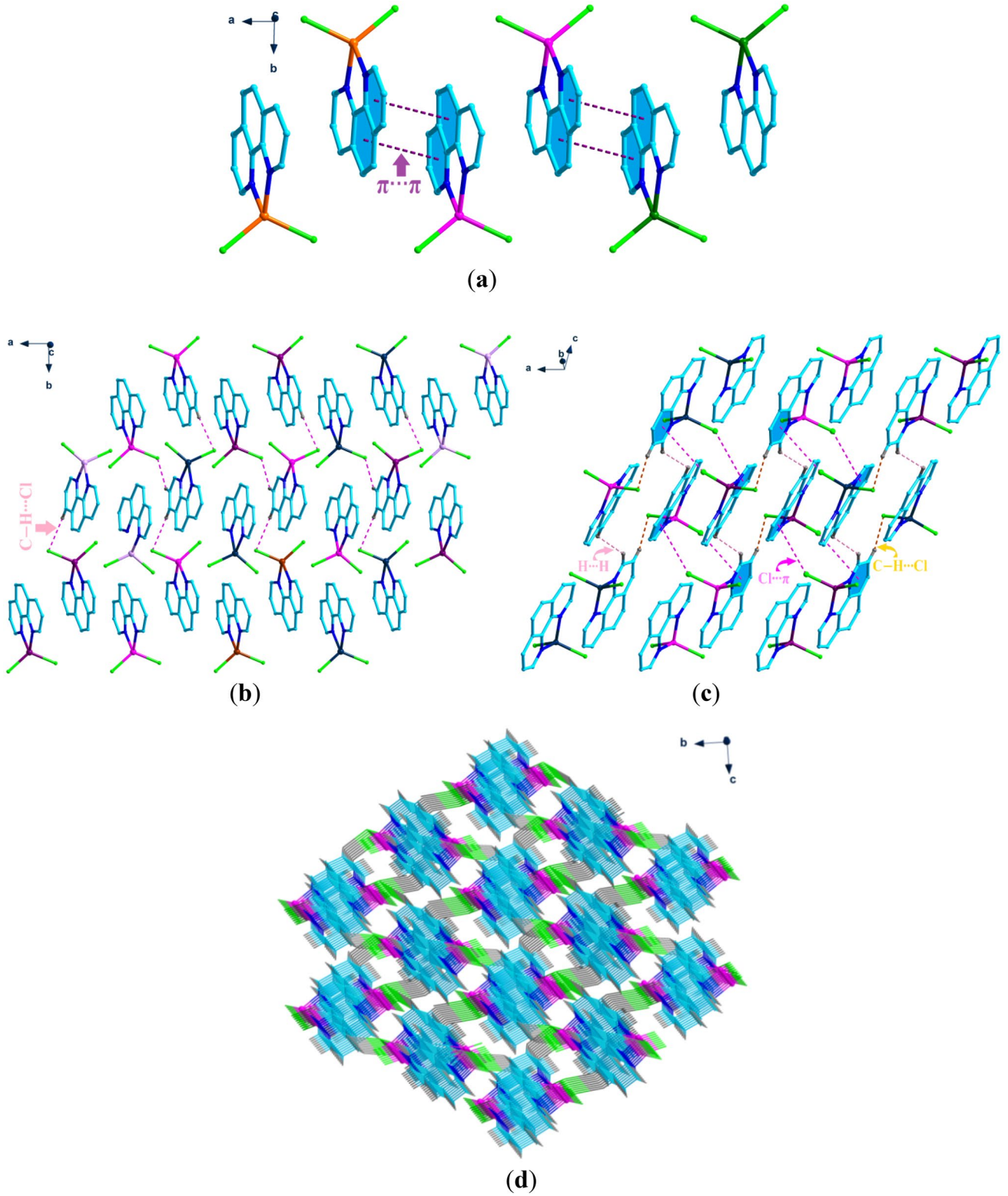


Fig. 6 **a** π···π interactions-stabilized 1D chain of **2** along *a*-direction. New interactions between different supramolecular dimers are only shown. Interconnectivity of 1D chains of **2** in the *ab*-plane (**b**) and *ac*-plane (**c**) through C–H···Cl and C–H···H–C interactions. New interactions between neighboring 1D chains are only shown. Different dimers are represented by different colors of the metal centers. Irrelevant H-atoms are omitted for clarity. **d** View of 3D architecture of **2** along *a*-direction

Table 4 C–H···Cl hydrogen bonding parameters (Å and °) for **2**

D – H···A	d (D – H)	d(D – A)	d (H···A)	< (DHA)
C2–H2···Cl2[a]	0.930	3.599	2.925 (1)	130.52 (3)
C3–H3···Cl3[b]	0.930	3.694	2.821 (1)	156.83 (3)
C7–H7···Cl3	0.930	3.482	2.764 (1)	134.79 (3)
C19–H19···Cl2	0.930	3.563	2.799 (1)	154.43 (3)
C22–H22···Cl2[c]	0.930	3.660	2.925 (1)	130.52 (3)
C23–H23···Cl3[d]	0.930	3.548	2.830 (1)	134.91 (3)

Symmetry codes: a: x –1/2, –y + 1, z + 1/2; b: x –1/2, –y + 2, z + 1/2; c: x + 1/2, –y + 1, z –1/2; d: x + 1/2, –y + 2, z –1/2

ligand from a supramolecular dimer in a particular chain are involved in C–H···H–C interactions with the C24–H24 and C1–H1 moieties of the same ligand from two chains above and below that particular chain. Additional reinforcement to this layered structure is provided by another C–H···Cl interaction involving the C2–H2 moiety from one chain and the Cl2 ligand from an adjacent at a H···Cl distance of 2.93 Å. The stacking of layered structures of **2,** in a very much similar way as **1**, gives rise to a 3D architecture of **2** along *a*-direction (Fig. 6d).

Hirshfeld surface analysis

The Hirshfeld surfaces were analyzed for the identification and quantification of the main intermolecular interactions and for a better understanding of the overall packing patterns of compounds **1** and **2**. The Hirshfeld surfaces of **1** and **2** are shown in Fig. 7, illustrating surfaces that have been mapped over d_{norm} property. The dominant interactions in the structure of both compounds are visible as bright red areas. The important quantitative information of the main intermolecular contacts in both compounds was obtained by plotting 2D fingerprint plots (full and decomposed) shown in Fig. 8. The full 2D FP plots include all intermolecular contacts, whereas decomposed FP plots depict specific intermolecular contacts.

In compound **1**, the red spots labeled 1 in the HSs are attributed to C–H···π interactions, involving the H27 atom of one phenyl ring and the C11 of the C9–C11 ring [d(H27···C11) = 2.765 Å]. These C–H···π contacts are visible as a pair of wings in the top left and bottom right region in the FP plots, which comprise 32.0% of the total Hirshfeld surface area. The H···O/O···H contacts in compound **1** are visible in the HSs as white areas around the O and H-atoms of the aromatic rings. The white color observed for these interactions is an indicative of weak contacts, in accordance with the H···O distances close to the sum of vdW radii of H and O-atoms. The proportion of H···O/O···H interactions comprises 19.3% of the total Hirshfeld surface. The bright red spots labeled 2 in the Hirshfeld surfaces are mainly attributed to Zn2–O8 coordination bond that interconnects the Zn-atoms. These close contacts appear as two symmetrical spikes at $(d_e + d_i) \approx 2.0$ Å and comprise 3.1% of the total HS area.

In compound **2**, the red spots labeled 1 and 3 in the HSs are attributed to C19–H19···Cl2 and C7–H7···Cl3 hydrogen bonds, respectively. These weak C–H···Cl hydrogen bonds are responsible for the stability of the two different molecules in the asymmetric unit. In addition, the visible red areas labeled 2 and 4 in the d_{norm} surfaces (Fig. 7) are mainly attributed to intermolecular C22–H22···Cl2 and C2–H2···Cl2 hydrogen bonds. These contacts are also visible in the 2D fingerprint plots as a pair of symmetrical spikes at $(d_e + d_i) \approx 2.6$ Å, contributing 42% to the total Hirshfeld surface area.

The calculations of the HSs reveal that in both compounds, the H···H contacts contribute to the crystal packing, with a proportion of 35.1 and 24.0% for **1** and **2**, respectively. These dihydrogen interactions are also visible in the FP plots (Fig. 8) in the middle of scattered points, with minimum values of $(d_e + d_i) \approx 2.35$ Å for both compounds.

We have mapped the Hirshfeld surfaces with shape index and curvedness properties (Fig. 9) in order to identify the regions involved in planar π···π stacking interactions. The pattern of red and blue triangles (highlighted by black dashed circles) on the same region of the shape index surface of both compounds is characteristic of π···π stacking interactions (Fig. 9, column 1). These contacts are also visible as relatively large and green flat regions delineated by black circles on the curvedness surfaces of both compounds (Fig. 9, column 2). Finally, the fingerprint plot of compound **2** (Fig. 8) shows the C···C contacts as a region of blue/green region on the diagonal around $d_e \approx d_i \approx 1.8$ Å.

Theoretical study of noncovalent interactions

As was mentioned above, the supramolecular assembly of compound **1** is mainly stabilized by C–H···O hydrogen bonds and unconventional noncovalent interactions such as π···π stacking and lone pair (lp) O···π interactions. Here, the lp O···π interaction is generated involving the O3 atom of the carboxylate group and the C12 atom of the phenyl ring as electron acceptor.

To study the noncovalent interactions observed in the solid-state structure of **1**, we have generated a monomeric model to facilitate the theoretical study by using simple monomers and dimers. The theoretical model used in this study is shown in Fig. 10, where we have removed the Zn(2) atom, and the carboxylate groups have been protonated to preserve the charge balance of the system. The supramolecular assembly of compound **2** is mainly stabilized by C–H···Cl hydrogen bonds, lp Cl···π and π···π stacking interactions.

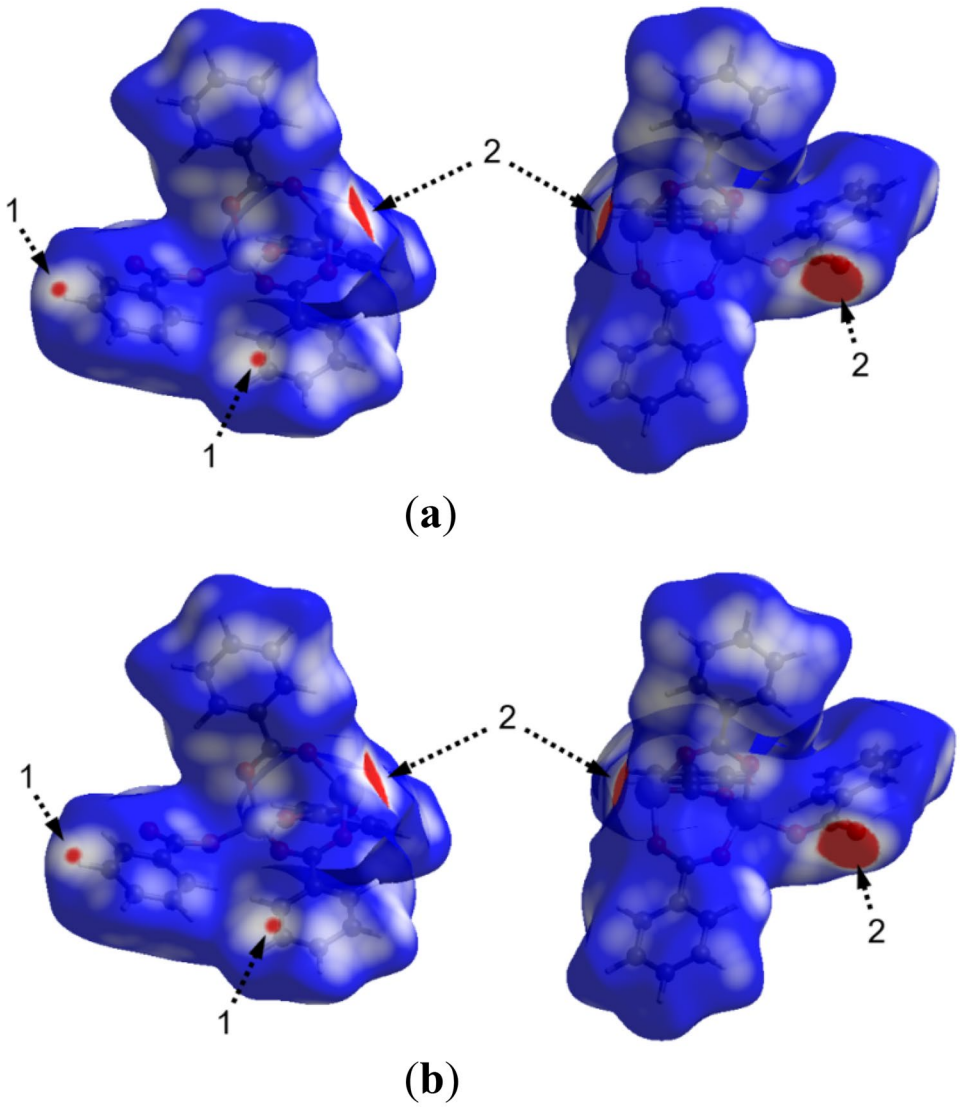


Fig. 7 Hirshfeld surfaces of compounds **1** (**a**) and **2** (**b**) mapped over d_{norm} property in two orientations. The second molecule is 180º rotated around the horizontal axis of the plot. These surfaces were mapped over a fixed color scale of −0.05 a.u. (red) to +0.5 a.u. (blue). The labels are discussed in the text

First, we computed the MEP surfaces of compounds **1** and **2** (Fig. 11). The surface of the model of **1** shows that the MEP minimum is located at the O-atom of the carboxyl group that is not coordinated to the Zn(II) center. The MEP maximum is located at the H-atom located at the para-position with respect to the carboxylate group, thus indicating that the C−H···O hydrogen bonds between these groups are favored electrostatically. It is interesting to note that the MEP is positive over one aromatic ring and negative at the other one, thus favoring the antiparallel π···π stacking interactions. These results are indicative that the π-stackings are relevant contacts in the crystal packing of **1**.

The MEP surface of **2** shows that the MEP maxima are located at the aromatic C−H bonds of the phenanthroline ligand, while the MEP minima are located at the chlorine atoms coordinated to the Zn(II) center. This analysis and the location of the MEP maxima and minima agree well with the important C−H···Cl interactions described above, which are crucial in the supramolecular assembly of compound **2**. As shown in Fig. 11, the MEP value is also positive over the center of the pyridine ring, thus indicating that the lone pair O···π interactions can be attractive in terms of electrostatic forces.

Figure 12 shows the combined QTAIM/NCI plot analysis of a theoretical model of **1** shown in Fig. 10. The dimerization energy is large (ΔE = − 14.23 kcal/mol) in line with the MEP surface shown in Fig. 11, since the most positive and negative regions of the complex interact upon the formation of the self-assembled dimer. The QTAIM analysis confirms the existence of C−H···O hydrogen bonds depicted in Fig. 12 that are characterized by bond critical points (labeled as 1 and 2) and bond paths interconnecting the H and O-atoms. The NCI plot index surface analysis also shows green isosurfaces between the H and O atoms coincident with the location of the bond critical points, thus indicating the weak attractive nature of these H-bonds. The

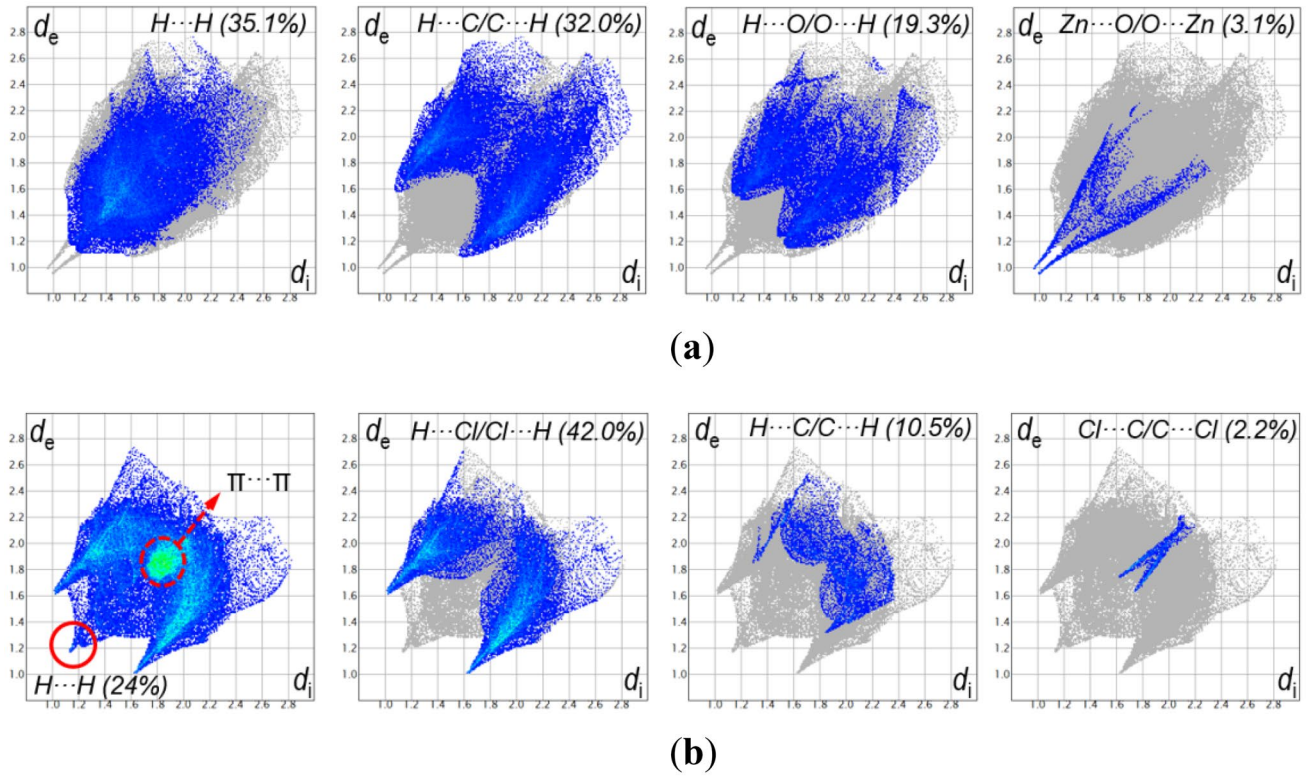


Fig. 8 Full and decomposed 2D fingerprint plots of compounds **1** (**a**) and **2** (**b**)

antiparallel π···π stacking interaction is characterized by two symmetrically equivalent bond critical points that interconnect the C-atoms of the phenyl ring. The π···π stacking contacts are confirmed by the presence of an extended green isosurface located between both aromatic rings. In addition, the presence of O···π interactions is also confirmed by the presence of two equivalent bond critical points and bond paths interconnecting the O and C-atoms of the phenyl ring.

The contribution of the C−H···O interactions has been estimated using the potential energy density at the bond critical point (V_r) and the formula proposed by Espinosa and co-workers ($E_{dis} = -0.5\ V_r$) [81]. The calculations indicate that the dissociation energy (E_{dis}) of the C12-H12···O6 (bond CP labeled 1) and C13−H13···O3 [bond CP labeled 2] hydrogen bonds are 0.596 and 0.376 kcal/mol, respectively. These results indicate that the C12−H12···O6 hydrogen bond is the strongest interaction, in accordance with the lowest H12···O16 distance of 2.904 Å as determined by X-ray diffraction methods. The QTAIM/NCI plot analysis discloses the existence of C−H···O contacts that are very weak, thus confirming that the formation of this dimer is mainly dominated by O···π and π···π stacking interactions.

As was described previously, the crystal structure of compound **2** shows two molecules in the asymmetric unit. The self-assembled of both molecules is generated by C−H···Cl hydrogen bonds and π···π stacking interactions between the aromatic rings of the *1,10*-phananthroline ligand. We have used a combination of QTAIM and NCI plot analysis to analyze the non-covalent interactions that play crucial roles in the stabilization of the molecules in the unit cell (Fig. 13a). The combined QTAIM/NCI plot analysis evidence that each C−H···Cl hydrogen bond is characterized by a bond CP (CP1-CP4) and bond paths interconnecting the H and Cl-atoms. The existence of C−H···Cl interactions is also characterized by green NCI plot isosurfaces coincident with the bond CPs, indicating the weak nature of these contacts. In addition, the distribution of bond CPs and bond paths shows that the π···π stacking interactions are characterized by four bond CPs and bond paths interconnecting the phenanthroline moieties (Fig. 13a). These interactions are also characterized by the presence of a green and extended isosurface located between the aromatic rings, thus confirming the attractive nature of the interactions. The dimerization energy is large and negative ($\Delta E = -22.34$ kcal/mol) due to the contribution of both the π···π and C−H···Cl hydrogen bonds.

Figure 13b shows the combined QTAIM/NCI plot analysis of a dimer of **2** stabilized by a combination of Cl···π and Cl···Cl halogen bonding interactions. The existence of such a combination of interactions is confirmed by both QTAIM and NCI plot index analysis and the corresponding bond CPs and green isosurfaces, supporting the modest dimerization energy ($\Delta E_1 = -6.621$ kcal/mol). The other self-assembled dimer of

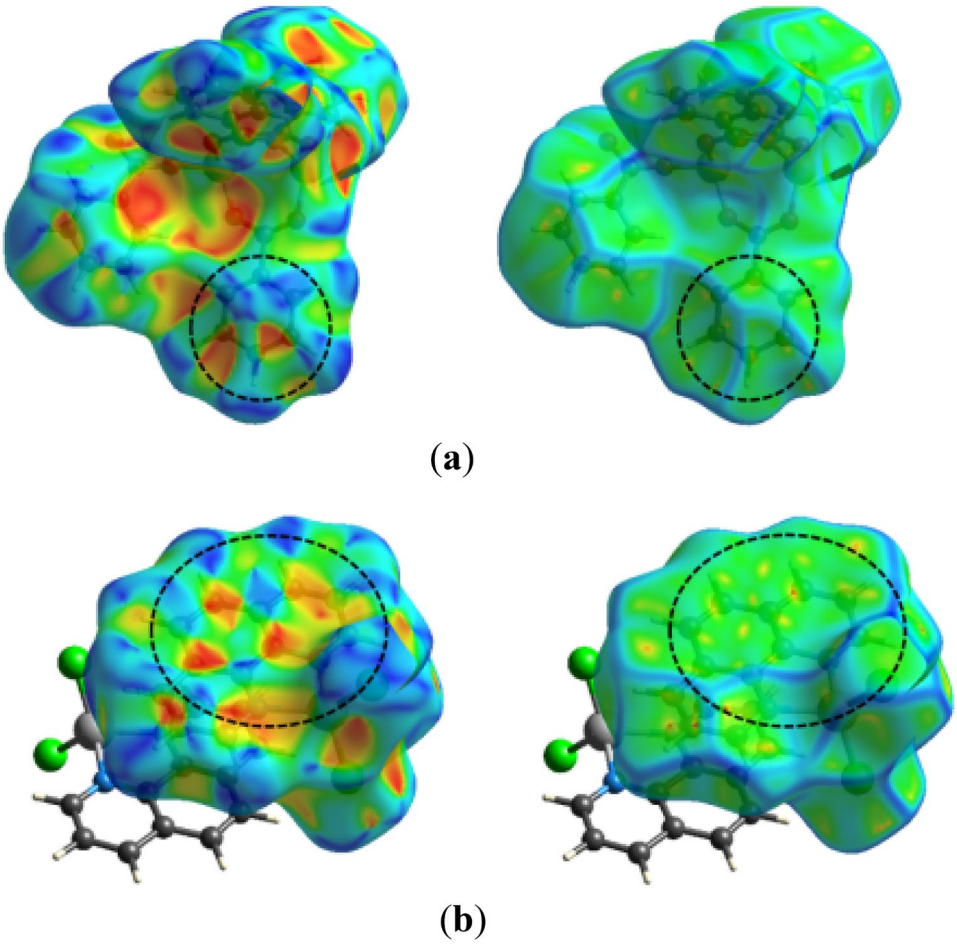


Fig. 9 Hirshfeld surfaces of **1** (**a**) and **2** (**b**) mapped over shape index and curvedness properties

2 is represented in Fig. 13c, where each C−H···Cl hydrogen bond is characterized by a bond CP and the bond path connecting the H-atoms of the aromatic rings and the Cl-atoms coordinated to the Zn(II) center. In addition, the shape of the NCI plot isosurface, embracing the whole π-system of the phenanthroline ligand, confirms the existence and attractive nature of the π···π stacking interaction. Such a combination of interactions explains the obtained large dimerization energy ($\Delta E_2 = -18.97$ kcal/mol).

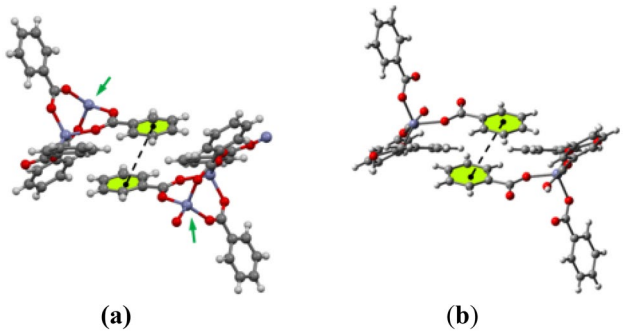


Fig. 10 **a** Partial view of the X-ray structure of **1**, showing the supramolecular assembly stabilized by different noncovalent interactions including lp O···π and π···π stacking interactions. **b** Theoretical model of **1** used for the study of noncovalent interactions

ADMET properties

The pharmacokinetic and toxicologic features such as absorption, distribution, metabolism, excretion, and toxicity (ADMET) for complexes **1** and **2** are summarized

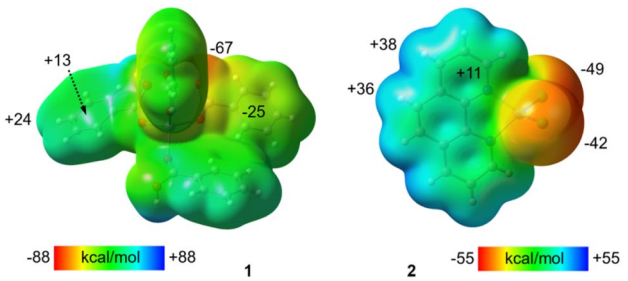


Fig. 11 MEP surfaces of compounds **1** and **2** (isovalue: 0.001 a.u.) computed at B3LYP-D3/def2-TZVP. The energies at the selected points are given in kcal/mol

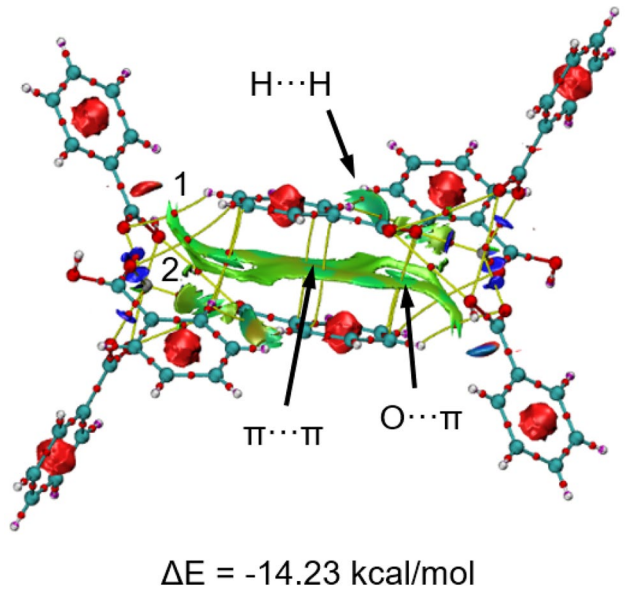


Fig. 12 Combination of QTAIM (bond critical points and bond paths represented as red spheres and yellow lines, respectively) and NCI plot of the dimer of **1**. The dimerization energy (kcal/mol) is also indicated

in Table 5. Both molecules have a high rate of absorption in the gastrointestinal system. It demonstrates that these molecules may be easily absorbed into the gastrointestinal system when administered orally. The results show that complex **1** does not have the potential to cross the BBB in the central nervous system and complex **2** has the potential to cross the BBB in the central nervous system. In the boiled egg model, the blue dot seen in the egg white for complex **1** and the yolk for complex **2** indicates that the complexes can be used as substrates for P-glycoprotein (Fig. 14). Although complex **1** is a non-inhibitor of the enzymes CYP1A2, CYP2C19, CYP2C9, CYP2D6, and CYP3A4 enzymes. While complex **2** is the non-inhibitor of CYP2C19 and CYP2C9, it is the inhibitor of CYP2D6, CYP1A2, and CYP3A4 enzymes. Complex **1** deviates from Lipinski's five rules and Ghose's rules only because of its molecular weight, which is greater than 500 $gmol^{-1}$, while complex **2** has properties compatible with Lipinski's five rules.

The pharmacokinetic and toxicologic features such as absorption, distribution, metabolism, excretion, and toxicity (ADMET) for complexes **1** and **2** are summarized in Table 5. Both molecules have a high rate of absorption in the gastrointestinal system. It demonstrates that these molecules may be easily absorbed into the gastrointestinal system when administered orally. The results show that complex **1** does not have the potential to cross the BBB in the central nervous system and complex **2** has the potential to cross the BBB in the central nervous system. In the boiled egg model, the blue dot seen in the egg white for complex **1** and the yolk for complex **2** indicates that the complexes can be used as substrates for P-glycoprotein (Fig. 14). Although complex **1** is a non-inhibitor of the enzymes CYP1A2, CYP2C19, CYP2C9, CYP2D6, and CYP3A4 enzymes. While complex **2** is the non-inhibitor of CYP2C19 and CYP2C9, it is the inhibitor of CYP2D6, CYP1A2, and CYP3A4 enzymes. Complex **1** deviates from Lipinski's five rules and Ghose's rules only because of its molecular weight, which is greater than 500 $gmol^{-1}$, while complex **2** has properties compatible with Lipinski's five rules.

Both complexes have properties compatible with Veber's and Egan's rules. The toxicity class of complex **1** was estimated as 3 and complex **2** as 4. However, according to data from the ProTOX-II online database, both complexes are hepatotoxic and carcinogenic, mutagenic, immunotoxic, cytotoxic, and irritant inactive. Finally, the predicted results show that these compounds have a reasonable ADMET characteristic and drug-likeness.

Molecular docking results

The SARS-CoV-2 virus has four structural proteins: envelope (E), membrane (M), nucleocapsid (N), and spike (S). Inhibiting one or more of these proteins will stop or delay the Coronavirus's effects [82]. The entry of coronavirus into cells begins with the binding of spike glycoprotein to the cell surface receptor angiotensin-converting enzyme 2 (ACE-2). Therefore, it is important to inhibit this protein [83]. In coronavirus drug research, other important targets are main proteinase (M^{pro}) and papain-like protease (PL^{pro}). Main proteinase (M^{pro}) and papain-like protease (PL^{pro}) are proteins that contribute greatly to replication and transcription in the viral replication cycle of the coronavirus [84]. Complexes **1** and **2** were docked to SARS-CoV-2 important proteins (spike protein of first and Omicron variant, main protease, papain-like protease, NSP12-NSP7-NSP8 complex, NSP15 Endoribonuclease, NSP16-NSP10 heterodimer, and transmembrane protease) (Figs. 15 and 16), and their binding energies and their ligand efficiencies were calculated (Table 5). Complex **1** has a higher binding affinity to all identified targets compared to **2**. Interestingly enough, these scores (for **1** vis-à-vis spike protein of Omicron variant and main protease, M^{pro}) are better than the corresponding scores for common antiviral drugs [85]. When evaluated in terms of binding affinity to the first variant and Omicron variant of the coronavirus, it was determined that complex **1** had a stronger binding affinity to the spike protein of the Omicron

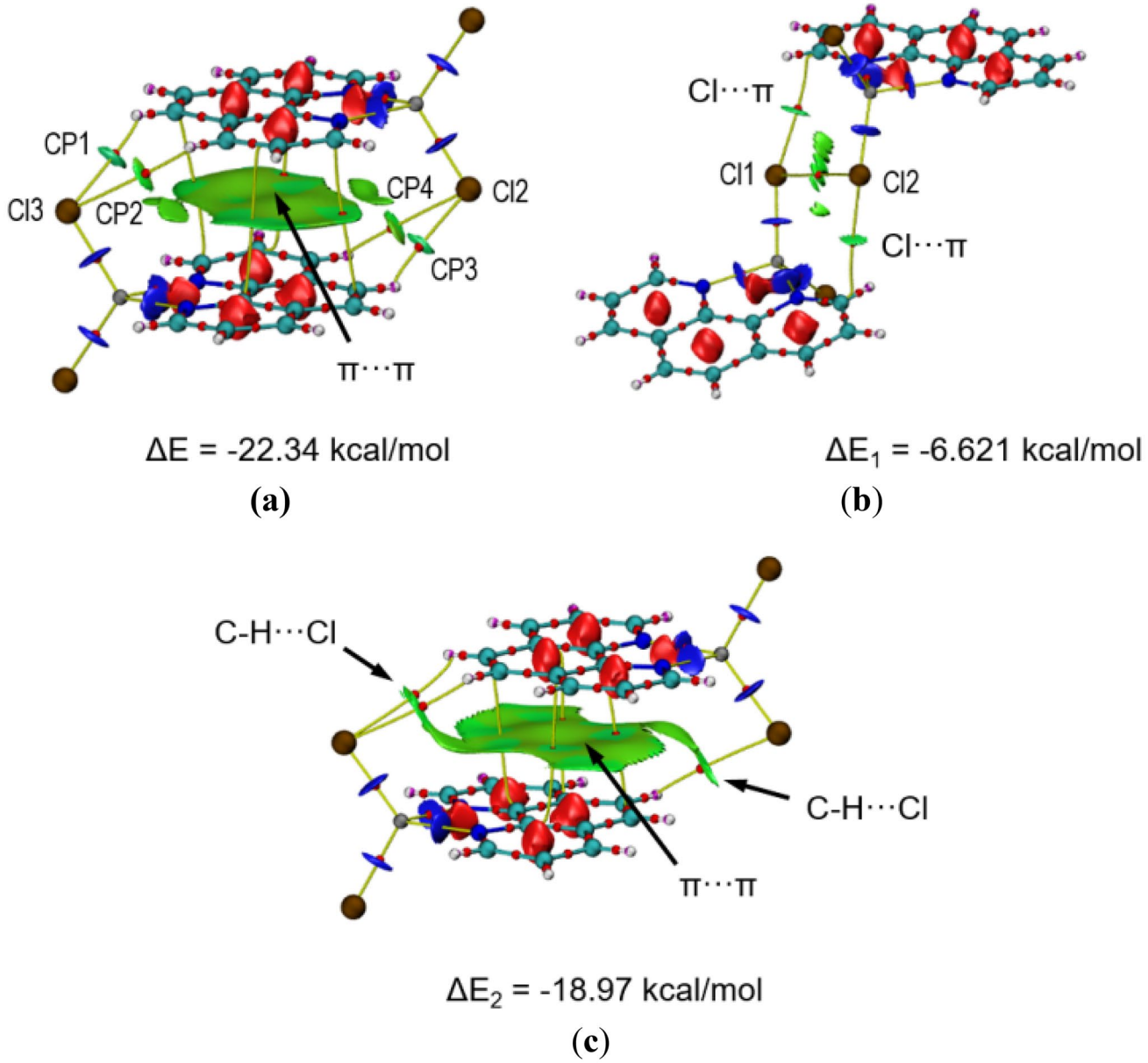


Fig. 13 Combination of QTAIM/NCI plot analysis of both molecules in the asymmetric unit (**a**) and the self-assembled dimers generated by lone pair Cl···π (**b**) and a combination of C-H···Cl and π···π stacking interactions (**c**). The bond critical points (CPs) are represented as red spheres and bond paths as yellow lines

variant, while complex **2** had a stronger binding affinity to the spike protein of the first variant. Complex **1** has a binding value of −7.50 kcal/mol for the main protease and −7.40 kcal/mol for the papain-like protease, which is required for viral replication and transcription. The binding energy values of complex **2** to the main protease and papain-like protease are −6.2 kcal/mol and −5.3 kcal/mol, respectively. It was determined that the binding affinity of both complexes to NSP15 Endoribonuclease is very strong when compared to their binding affinities to other proteins. The complexes were determined to bind to the spike protein of the first and Omicron variant, main protease, papain-like protease, NSP12-NSP7-NSP8 complex, NSP15 endoribonuclease, NSP16-NSP10 heterodimer, and transmembrane protease proteins of coronavirus via interactions such as hydrogen bond, π-donor hydrogen bond,

Table 5 The pharmacokinetic properties of **1** and **2**

Properties	Complex 1	Complex 2
Molecular weight[a]	615.22 $gmol^{-1}$	316.49 $gmol^{-1}$
Heavy atoms	40	17
Rotatable bonds	6	0
H-bond acceptors	9	0
H-bond donors	0	0
Molar refractivity	128.12	68.75
TPSA ($Å^2$)	105.20	9.86
Log $P_{o/w}$	2.24	2.39
GI absorption	High	High
BBB permeant	No	Yes
P-gp substrate	Yes	Yes
CYP1A2 inhibitor	No	Yes
CYP2C19 inhibitor	No	No
CYP2C9 inhibitor	No	No
CYP2D6 inhibitor	No	Yes
CYP3A4 inhibitor	No	Yes
Log K_p (cm/s)	−5.44	−5.49
Lipinski	Yes, 1 violation MW > 500	Yes, 0 violation
Ghose	No, 1 violation MW > 480	Yes
Veber	Yes	Yes
Egan	Yes	Yes
Toxicity class[a]	3	4
Predicted LD_{50}	290 $mgkg^{-1}$	1035 $mgkg^{-1}$
Hepatotoxicity	Inactive	Inactive
Carcinogenicity	Inactive	Inactive
Immunotoxicity	Inactive	Inactive
Mutagenicity	Inactive	Inactive
Cytotoxicity	Inactive	Inactive
MMP[b]	Inactive	Inactive
Irritant	Inactive	Inactive

[a]The toxicity class consists of six numbers (Number 1 means toxic; number 6 means non-toxic.)

[b]*MMP* mitochondrial membrane potential

carbon hydrogen bond, π-π stacked, π-alkyl, attractive charge, π-anion, π-sigma, π-cation, π-π T-shaped, amide-π interactions, alkyl, metal-acceptor, π-sulfur. Complex **1** interacts with the nonstructural proteins of the coronavirus by conventional hydrogen bonds. Complex **1** interacts by conventional hydrogen bonds with arg553 amino acid in the active site of the NSP12-NSP7-NSP8 complex, asp268 and gln202 amino acid in the active site of NSP15 endoribonuclease, and ser7090 amino acid in the active site of the NSP16-NSP10 heterodimer. These hydrogen bond distances are 2.76, 3.38, 2.37, and 2.43 Å, respectively. Complex **2** is bonded by conventional hydrogen bond with amino acid residues lys105, asn110, thr265, and his272 in the active site of the protease, such as papain. The bond distances between complex **2** and amino acids lys105, asn110, thr265, and his272 were found as 2.05, 2.29, 2.06, and 1.77 Å, respectively. Given these findings, it is thought that complex **1** is suitable for non-covalent interactions and will have a positive inhibitory effect when interacting with coronavirus enzymes.

Thermal analysis

The thermal stabilities of **1** and **2** were examined by their thermal analyses (TGA/DTG) in a temperature range of 25–700 °C under N_2 atmosphere at a heating rate of 10 °C min^{-1}. As shown in Fig. 17, the DTG curve shows a mass loss of **1** in three steps. The 75.90% mass loss occurring between 99 and 500 °C is attributed to the release of four coordinated benzoato ligands per formula unit of **1** (calc. = 78.76%). The final weight is approximately 24.10%, suggesting the predominance of 2[ZnO] (calc. = 26.46%). For **2**, the 77.59% weight loss up to 400 °C corresponds to the loss of the coordinated *1,10*-phenanthroline and the two chlorido ligands (calc. = 79.34%).

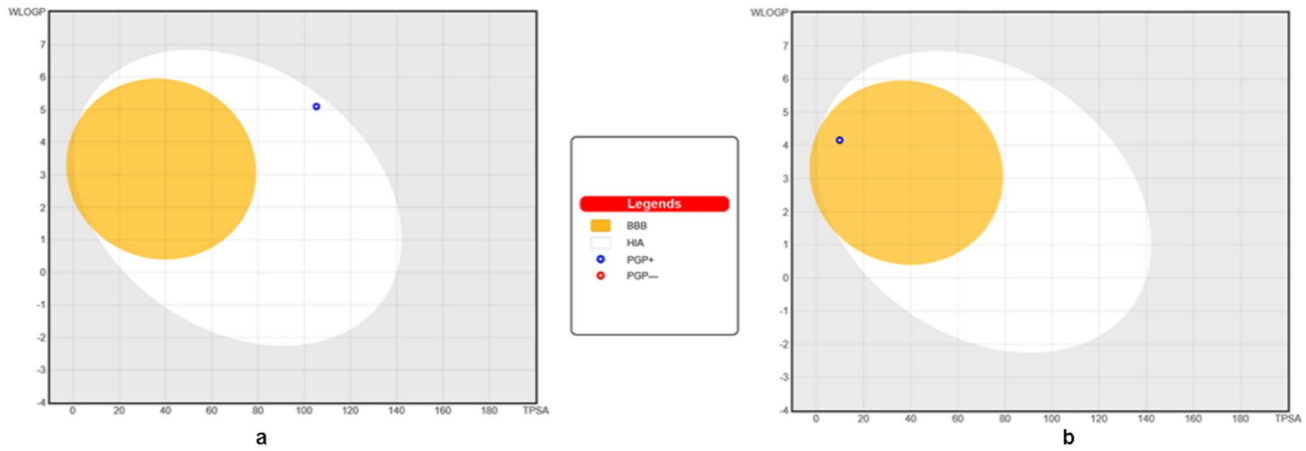


Fig. 14 Boiled egg model for complex **1** (**a**) and complex **2** (**b**)

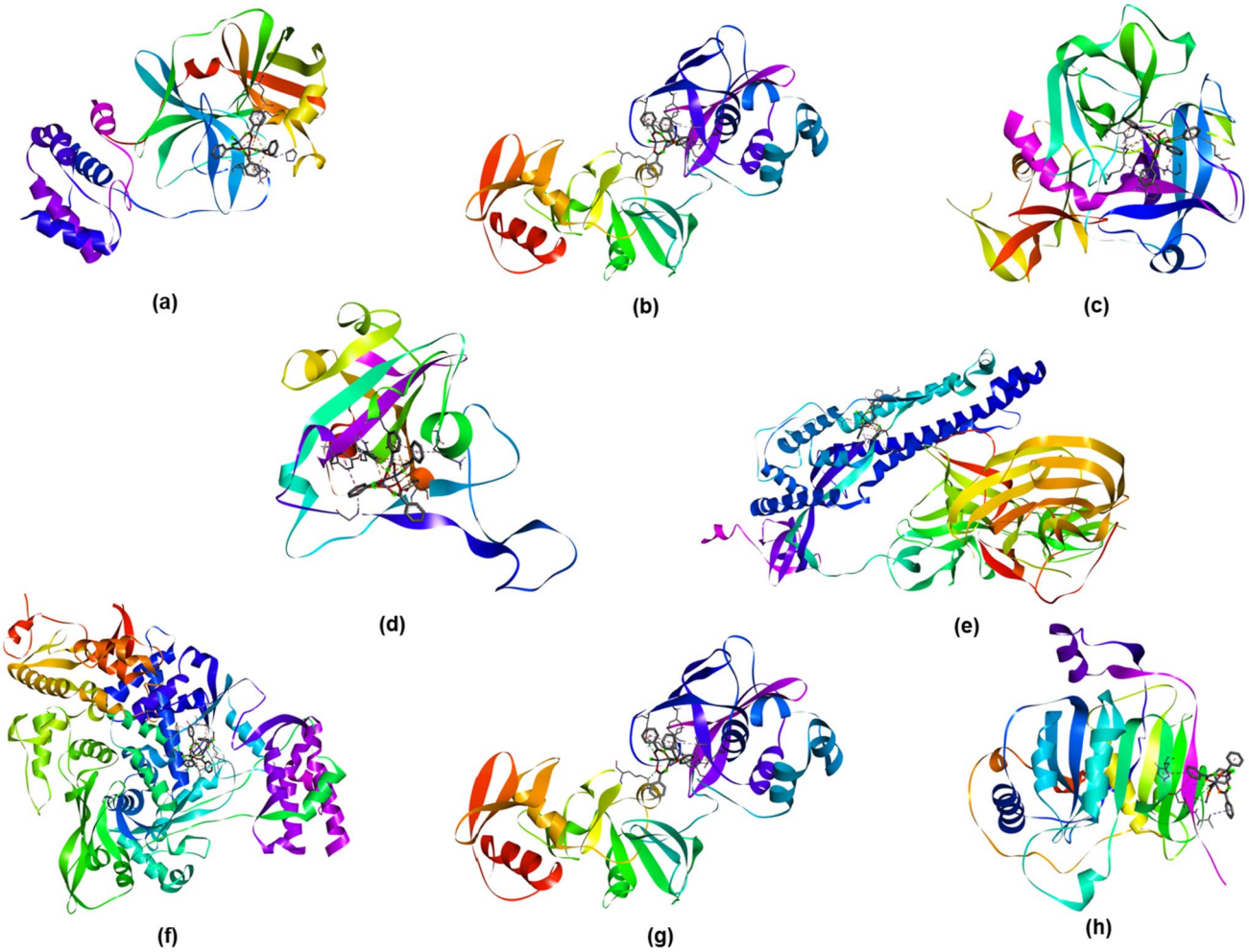


Fig. 15 The molecular docking results of complexes **1** on the main protease (**a**), papain-like protease (**b**), transmembrane protease (**c**), spike protein of first variant (**d**), spike protein of Omicron variant (**e**), NSP12-NSP7-NSP8 complex (**f**), NSP15 Endoribonuclease (**g**), and NSP16-NSP10 heterodimer (**h**)

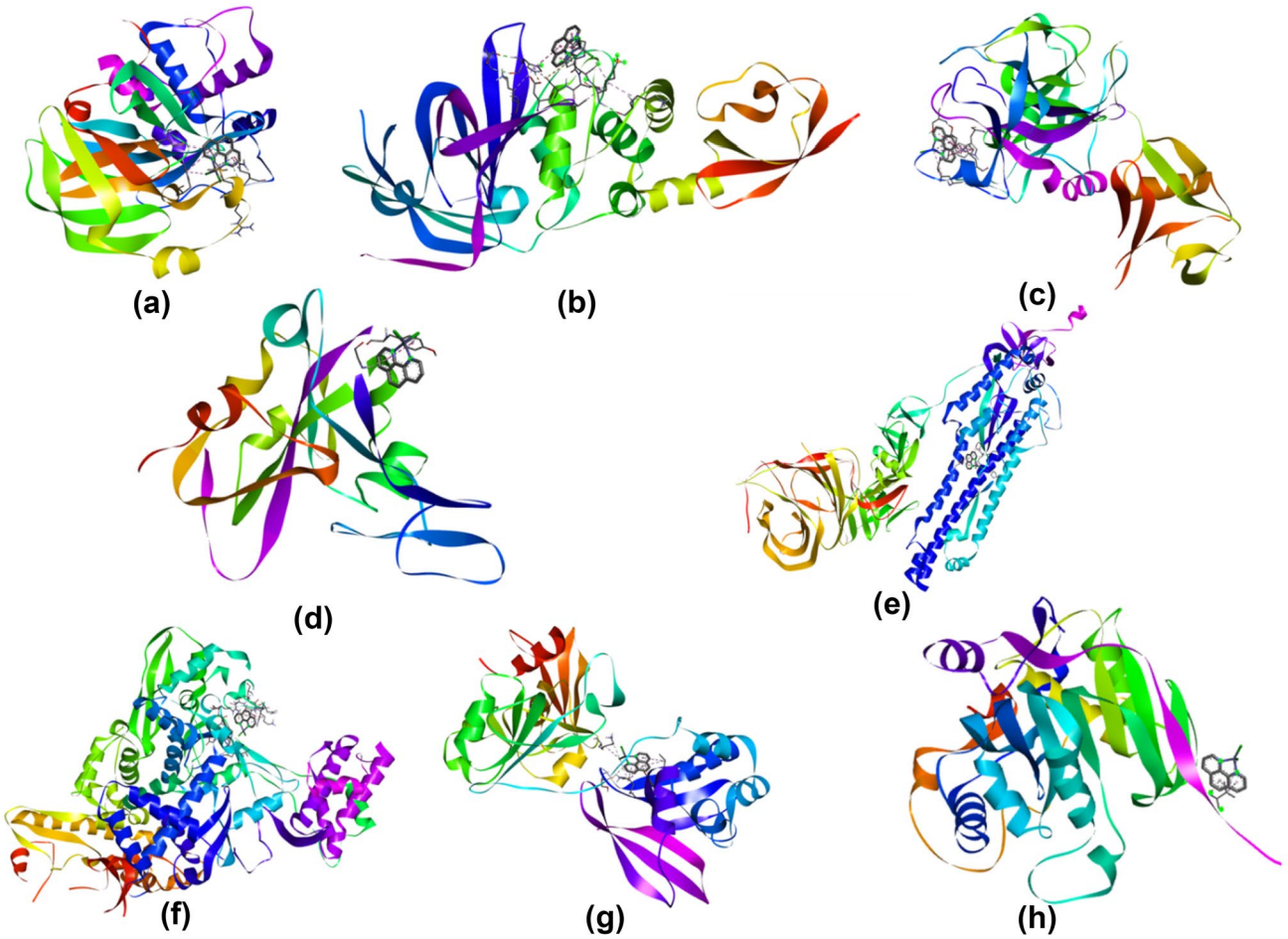


Fig. 16 The molecular docking results of complexes **2** on the main protease (**a**), papain-like protease (**b**), transmembrane protease (**c**), spike protein of first variant (**d**) spike protein of Omicron variant (**e**), NSP12-NSP7-NSP8 complex (**f**), NSP15 Endoribonuclease (**g**), and NSP16-NSP10 heterodimer (**h**)

Table 6 Binding energies and ligand efficiencies of **1** and **2**

Protein (PDB ID)	Complex	Interaction Type				Docking Score (kcal/mol)	Ligand Efficiency
		Hydrogen Bonding	Hydrophobic	Electrostatic	Other		
6M0J	**1**	: Gly496	: Tyr505 : Lys417	: Arg403, Tyr453		−7.50	−0.19
	2	: Gly496	: Tyr505 : Tyr505			−5.80	−0.34
7T9J	**1**	:His1058 :His1058	: Leu861 : Val952, Pro863, Ile870, Pro1057, Pro862	: His1058, : His1058		−7.70	−0.19
	2	: Asp867	: His1058 : Pro863 : His1058, Pro1057, Val952	: His1058		−5.10	−0.30
7BQY	**1**		: Val186, Met82	: Arg40, Arg188 : Arg40, Arg188	: Pro52	−7.50	−0.19
	2	: Arg188	: Gln189 : His41 : Met165, Met49, Cys145, Met165, His41			−6.20	−0.36
6W9C	**1**	: His272 : His272	: Trp106 : Cys270, Leu289	: His272 : Trp106, His272	: Asn109	−7.40	−0.19
	2	:Lys105, Asn110, Thr265, His272 : Asn109	: Trp106, His272 : Lys94, Ala288, Lys505 : His272, Cys111	: His272 : Cys111		−5.30	−0.31

Table 6 (continued)

7BV2	**1**	: Arg553	: Cys622, Lys551, Pro620, Lys798	: Arg553 : Asp618, Asp760	: Asp618	−8.50	−0.21
	2		: Lys500, Ala512	: Arg569		−5.50	−0.32
6WXC	**1**	: Asp268, Gln202 : Lys90 : Tyr279	: Leu201, Leu252, Lys277	: Lys90, Asp298		−9.00	−0.23
	2	: Lys90, Ser274, Tyr279	: Tyr279 : Lys90, Lys277 : Lys277, Leu252			−7.40	−0.44
6WKQ	**1**	: Ser7090	: Val7092 : His6917	: Asp7091	: Ser7090	−5.30	−0.13
	2	: Val7092	: Val7092, : Val7092			−4.30	−0.25
7MEQ	**1**	: Lys342	: Trp461 : Trp461 : Lys342	: His296, Lys342 : Lys342 : Cys465		−8.60	−0.22
	2	: Ser463	: Trp461 : Leu419 : Lys342, Tyr416, Trp461			−6.0	−0.35

:Hydrogen Bond, : π-Donor Hydrogen Bond, : Carbon Hydrogen Bond, : π- π Stacked, : π-Alkyl, :Attractive Charge, : π-Anion, : π-Sigma, : π-Cation, : π- π T-shaped, : Amide-π Interactions, : Alkyl, : Metal-Acceptor, : π-Sulfur

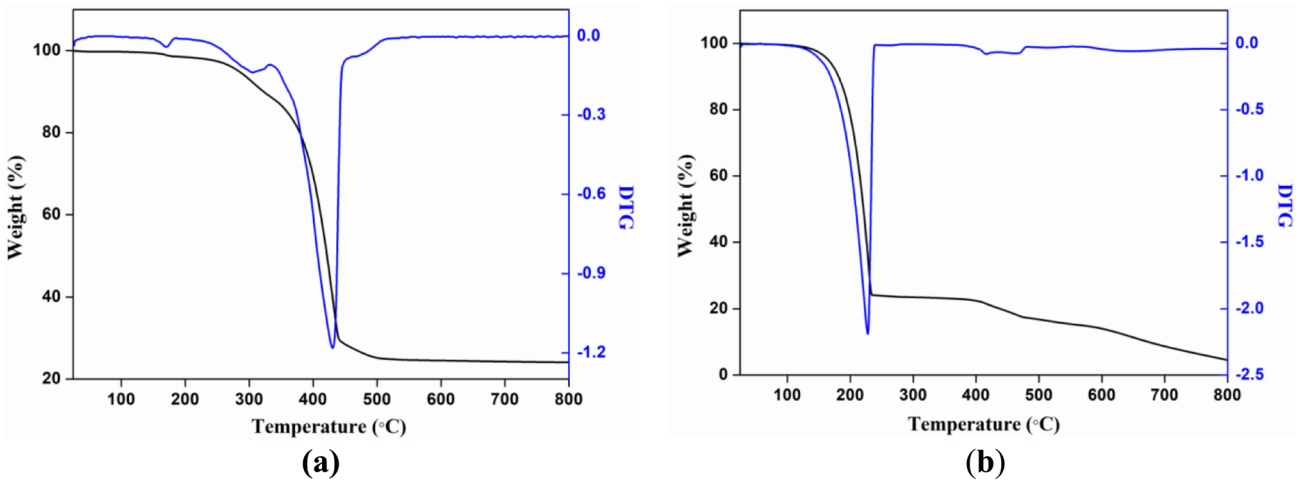


Fig. 17 The TG-DTG curves of **1** (**a**) and **2** (**b**)

Conclusions

Two tetrahedral complexes of Zn(II) involving bridging benzoato (Bz) and *1,10*-phenanthroline (Phen) ligands viz. $[Zn_2(\mu_2\text{-}Bz)_3]_n$ (**1**) and $[Zn(Phen)Cl_2]_2$ (**2**) were synthesized at room temperature and characterized by single-crystal XRD, FT-IR, PXRD, and thermal analysis. Complex **1** is a coordination polymer with an unusual secondary building unit (SBU), whereas **2** is a novel supramolecular dimer with two "differently similar" monomers. In the solid state, the polymer **1** contains a basic dimeric unit, interlinking of which through a bridging benzoate ion in the *syn, syn*-$\eta^1{:}\eta^1{:}\mu_2$ coordination mode gives rise to a linear polymeric chain. These chains interconnect themselves in two perpendicular directions through π···π, C−H···O, C−H···H−C, and lone pair (lp)···π interactions to ultimately give a 3D architecture of **1**. The π···π interactions-stabilized supramolecular dimer in **2** self-assembles to a linear chain, interlinking of which, like **1**, in two perpendicular directions, through mainly C−H···Cl interactions, imparts a 3D architecture to **2**. This architecture is stabilized by lone-pair (Cl)···π interactions. Important supramolecular interactions in **1** and **2** contributing to their stability were studied by Hirshfeld surface analysis and other theoretical tools. The binding affinity of the complexes towards seven important SARS-CoV-2 proteins was investigated with molecular docking study. The results showed that binding affinities of **1** towards spike protein and M^{pro} of SARS-CoV-2 were higher than those for the common antiviral drugs such as chloroquine, hydroxychloroquine, and Remdesivir. ADMET calculations predicted good compliance of the complexes with both Lipinisk's and Veber's rules. As such, further investigation and experimentation of the synthesized complexes (particularly **1**) are recommended to validate their candidature as a therapeutic agent for COVID-19.

Supplementary Information The online version contains supplementary material available at https://doi.org/10.1007/s11224-024-02294-5.

Acknowledgements DMG is a member of the research career of CONICET. DMG thanks Secretaría de Ciencia, Arte e Innovación Tecnológica, SCAIT – UNT (Project D728), CONICET (PIP 215), and Agencia Nacional de Promoción Científica y Tecnológica, ANPCyT (PICT-serie A-02988) for financial support. The authors thank Dr. Antonio Frontera for the computational facility.

Author contribution Swah Mohd. Nashre-ul-Islam: conceptualization, software, writing—original draft, writing—review and editing. Kamala Kanta Borah: writing—review and editing. Füreya Elif Öztürkkan: software, writing—original draft. Pravin A. Dhakite: writing—review and editing. Muhammad Asam Raza: writing—review and editing. Diego M. Gil: software, writing—original draft.

Declarations

Conflict of interest The authors declare no competing interests.

References

1. Hui DS, David S, Memish ZA, Zumla A (2014) Curr Opin Pulm Med 20:233–241. https://doi.org/10.1097/MCP.0000000000000046
2. Boopathia S, Pomab AB, Kolandaivel P (2021) J Biomol Struct Dyn 39:3409–3418. https://doi.org/10.1080/07391102.2020.1758788
3. Chan JF-W, Kok K-H, Zhu Z, Chu H, To KK-W, Yuan S, Yuen K-Y (2020) Emerg microbes & infect 9:221–236. https://doi.org/10.1080/22221751.2020.1719902
4. Huang Y, Yang C, Xu X-F, Xu W, Liu S-W (2020) Acta Pharmacol Sin 41:1141–1149. https://doi.org/10.1038/s41401-020-0485-4
5. Shang J, Wan Y, Luo C, Ye G, Geng Q, Auerbach A, Li F (2020) Proc Acad Nat Sci 117:11727–11734. https://doi.org/10.1073/pnas.2003138117
6. Trougakos IP, Stamatelopoulos K, Terpos E, Tsitsilonis OE, Aivalioti E, Paraskevis D, Kastritis E, Pavlakis GN, Dimopoulos MA (2021) J Biomed Sci 28:1–18. https://doi.org/10.1186/s12929-020-00703-5
7. Zhou P, Yang X-L, Wang X-G, Hu B, Zhang L, Zhang W, Si H-R, Zhu Y, Li B, Huang C-L, Chen H-D, Chen J, Luo Y, Guo H, Jiang R-D, Liu M-Q, Chen Y, Shen X-R, Wang X, Zheng X-S, Zhao K, Chen Q-J, Deng F, Liu L-L, Yan B, Zhan F-X, Wang Y-Y, Xiao G-F, Shi Z-L (2020) Nature 579:270–273. https://doi.org/10.1038/s41586-020-2012-7
8. Xu X, Chen P, Wang J, Feng J, Zhou H, Li X, Zhong W, Hao P (2020) Sci China Life Sci 63:457–460. https://doi.org/10.1007/s11427-020-1637-5
9. Pillaiyar T, Manickam M, Namasivayam V, Hayashi Y, Jung S-H (2016) J Med Chem 59:6595–6628. https://doi.org/10.1021/acs.jmedchem.5b01461
10. Anand K, Ziebuhr J, Wadhwani P, Mesters JR, Hilgenfeld R (2003) Science 300:1763–1767. https://doi.org/10.1126/science.1085658
11. Chen Y, Liu Q, Guo D (2020) J Med Virol 92:418–423. https://doi.org/10.1002/jmv.25681
12. Shin D, Mukherjee R, Grewe D, Bojkova D, Baek K, Bhattacharya A, Schulz L, Widera M, Mehdipour AR, Tascher G, Geurink PP, Wilhelm A (2020) van der Heden van Noort GJ, Ovaa H, Müller S, Knobeloch K-P, Rajalingam K, Schulman BA, Cinatl J, Hummer G, Ciesek S, Dikic I. Nature 587:657–662. https://doi.org/10.1038/s41586-020-2601-5
13. Sacco MD, Ma C, Lagarias P, Gao A, Townsend JA, Meng X, Dube P, Zhang X, Hu Y, Kitamura N, Hurst B, Tarbet B, Marty MT, Kolocouris A, Xiang Y, Chen Y, Wang, (2020) J Sci Adv 6:eabe0751. https://doi.org/10.1126/sciadv.abe0751
14. Gao K, Wang R, Chen J, Tepe JJ, Huang W-W (2021) J Med Chem 64:16922–16955. https://doi.org/10.1021/acs.jmedchem.1c00409
15. Pal M, Musib D, Roy M (2020) New J Chem 45:1924–1933. https://doi.org/10.1039/D0NJ04578K
16. Pawełczyk A, Zaprutko L (2020) Future Med Chem 12:1743–1757. https://doi.org/10.4155/fmc-2020-0204
17. Anthony EJ, Bolitho EM, Bridgewater HE, Carter OWL, Donnelly JM, Imberti C, Lant EC, Lermyte F, Needham RJ, Palau M, Sadler PJ, Shi H, Wang F-X, Zhang W-Y, Zhang Z (2020) Chem Sci 11:12888–12917. https://doi.org/10.1039/D0SC90284E
18. Boros E, Dyson PJ, Gasser G (2020) Chem 6:41–60. https://doi.org/10.1016/j.chempr.2019.10.013
19. Mjos KD, Orvig C (2014) Chem Rev 114:4540–4563. https://doi.org/10.1021/cr400460s
20. Karges J (2020) ChemBioChem 21:3044–3046. https://doi.org/10.1002/cbic.202000397
21. Meier-Menches SM, Gerner C, Berger W, Hartinger CG, Keppler BK (2018) Chem Soc Rev 47:909–928. https://doi.org/10.1039/C7CS00332C
22. Karges J, Stokes RW, Cohen SM (2021) Trends Chem 3:523–534. https://doi.org/10.1016/j.trechm.2022.11.006

23. Weder JE, Dillon CT, Hambley TW, Kennedy BJ, Lay PA, Biffin JR, Regtop HL, Davies NM (2002) Coord Chem Rev 232:95–126. https://doi.org/10.1016/s0010-8545(02)00086-3
24. Karges J, Cohen SM (2021) ChemBioChem 22:1–9. https://doi.org/10.1002/cbic.202100186
25. Cirri D, Pratesi A, Marzo T, Messori L (2021) Expert Opin Drug Discovery 16:39–46. https://doi.org/10.1080/17460441.2020.1819236
26. de Paiva REF, Neto AM (2020) ISantos IA, Jardim ACG, Corbi PP, Bergamini FRG. Dalton Trans 49:16004–16033. https://doi.org/10.1039/D0DT02478C
27. Kumar S, Choudhary M (2023) New J Chem 232:116296. https://doi.org/10.1039/D3NJ01351K
28. Ahmed YM, Omar MM, Mohamed GG (2022) J Iran Chem Soc 19:901–919. https://doi.org/10.1007/s13738-021-02359-w
29. Al-Janabi ASM, Elzupir AO, Abou-Krisha MM, Yousef TA (2023) Inorganics 11:63. https://doi.org/10.3390/inorganics11020063
30. Yadav O, Kumar M, Mittal Yadav HK, Seidel V, Ansari A (2022) Front Pharmacol 13:982484. https://doi.org/10.3389/fphar.2022.982484
31. Read SA, Obeid S, Ahlenstiel C, Ahlenstiel G (2019) Adv Nutr 10:696–710. https://doi.org/10.1093/advances/nmz013
32. Ghaffari H, Tavakoli A, Moradi A, Tabarraei A, Bokharaei-Salim F, Zahmatkeshan M, Farahmand M, Javanmard D, Kiani SJ, Esghaei M, Pirhajati-Mahabadi V (2019) J Biomed Sci 26:1–10. https://doi.org/10.1186/s12929-019-0563-4
33. Pormohammad A, Monych NK, Turner RJ (2021) Int J Mol Sci 47:326–334. https://doi.org/10.3892/ijmm.2020.4790
34. Rahman MT, Idid SZ (2021) Biol Trace Elem Res 199:550–558. https://doi.org/10.1007/s12011-020-02194-9
35. Islam SMN, Dutta D, Sharma P, Verma AK, Frontera A, Bhattacharyya MK (2019) Inorganica Chim Acta 498:119108–119118. https://doi.org/10.1016/j.ica.2019.119108
36. Bhattacharyya MK, Dutta D, Islam SMN, Frontera A, Sharma P, Verma AK, Das A (2020) Inorganica Chim Acta 501:119233–119246. https://doi.org/10.1016/j.ica.2019.119233
37. Islam SMN, Dutta D, Verma AK, Nath H, Frontera A, Sharma P, Bhattacharyya MK (2019) Inorganica Chim Acta 498:119161–119174. https://doi.org/10.1016/j.ica.2019.119161
38. Islam SMN, Borah KK, Raza MA, Öztürkkan FE (2023) Polyhedron 233:116304–116316. https://doi.org/10.1016/j.poly.2023.116304
39. Bruker AXS Inc. (2007) Madison, Wisconsin, USA, 2007 Cross-Ref CAS PubMed; GM Sheldrick, A short history of SHELX. Acta Crystallogr Sect A Fundam Crystallogr 64:112–122
40. Bruker AXS Inc. (2001) Programme Name (s). Madison, Wisconsin, USA
41. Sheldrick GM (2008) Acta Crystallogr A 64:112–122
42. Farrugia LJ (1999) J Appl Crystallogr 32:837–838. https://doi.org/10.1107/S0021889812029111
43. Brandenburg K (2008) Diamond: Visual Crystal Structure Information System (Version 3.1f), Crystal Impact GbR, Bonn
44. Spackman MA, Byrom PG (1997) Chem Phys Lett 267:215–220. https://doi.org/10.1016/S0009-2614(97)00100-0
45. McKinnon JJ, Spackman MA, Mitchel AS (2007) Acta Crystallogr B 60:627–668. https://doi.org/10.1107/S0108768104020300
46. Spackman MA, Jayatilaka D (2009) CrystEngComm 11:19–32. https://doi.org/10.1039/B818330A
47. Islam SMN, Borah KK, Öztürkkan FE, Raza MA, Frontera A, Gil DM (2022) J Mol Struct 1268:133686–133698. https://doi.org/10.1016/j.molstruc.2022.133686
48. Spackman PR, Turner MJ, McKinnon JJ, Wolff SK, Grimwood DJ, Jayatilaka D, Spackman MA (2021) J Appl Cryst 54:1006–1011. https://doi.org/10.1107/S1600576721002910
49. Parkin A, Barr G, Dong W, Gilmore CJ, Jayatilaka D, McKinnon JJ, Spackman MA, Wilson CC (2007) CrystEngComm 9:648–652. https://doi.org/10.1039/B704177B
50. Frisch MJ, Trucks GW, Schlegel HB, Scuseria GE, Robb MA, Cheeseman JR, Scalmani G, Barone V, Mennucci B, Petersson GA, Nakatsuji H, Caricato M, Li X, Hratchian HP, Izmaylov AF, Bloino J, Zheng G, Sonnenberg JL, Hada M, Ehara M, Toyota K, Fukuda R, Hasegawa J, Ishida M, Nakajima T, Honda Y, Kitao O, Nakai H, Vreven T, Montgomery Jr. JA, Peralta JE, Ogliaro F, Bearpark M, Heyd JJ, Brothers E, Kudin KN, Staroverov VN, Keith T, Kobayashi R, Normand J, Raghavachari K, Rendell A, Burant JC, Iyengar SS, Tomasi J, Cossi M, Rega N, Millam JM, Klene M, Knox JE, Cross JB, Bakken V, Adamo C, Jaramillo J, Gomperts R, Stratmann RE, Yazyev O, Austin AJ, Cammi R, Pomelli C, Ochterski JW, Martin RL, Morokuma K, Zakrzewski VG, Voth GA, Salvador P, Dannenberg JJ, Dapprich S, Daniels AD, Farkas O, Foresman JB, Ortiz JV, Cioslowski J, Fox DJ (2013) Gaussian 09, Revision D.01
51. Grimme S, Antony J, Ehrlich S, Krieg H (2010) J Chem Phys 132:154104. https://doi.org/10.1063/1.3382344
52. Weigend F (2006) Phys Chem Chem Phys 8:1057–1065. https://doi.org/10.1039/B515623H
53. Bader RFW (1998) J Phys Chem 102:7314–7323. https://doi.org/10.1021/jp981794v
54. Lu T, Chen F (2012) J Comput Chem 33:580–592. https://doi.org/10.1002/jcc.22885
55. Contreras-Garcia J, Johnson E, Keinan S, Chaudret R, Piquemal J-P, Beratan D, Yang W (2011) J Chem Theory Comput 7:625–632. https://doi.org/10.1021/ct100641a
56. Humphrey W, Dalke A, Schulten K (1996) J Molec Graphics 14:33–38. https://doi.org/10.1016/0263-7855(96)00018-5
57. Lipinski CA, Lombardo F, Dominy BW, Feeney PJ (1997) Adv Drug Deliv Rev 23:3–25. https://doi.org/10.1016/S0169-409X(96)00423-1
58. Daina A, Michielin O, Zoete V (2017) Sci Rep 7:42717. https://doi.org/10.1038/srep42717
59. Banerjee P, Eckert AO, Schrey AK, Preissner R (2018) Nucleic Acids Res 46:W257–W263. https://doi.org/10.1093/nar/gky318
60. Trott O, Olson AJ (2009) Effic Optim Multithreading 31:455–461
61. Lan J, Ge J, Yu J, Shan S, Zhou H, Fan S, Zhang Q, Shi X, Wang Q, Zhang L, Wang X (2020) Nature 581:215–220. https://doi.org/10.1038/s41586-020-2180-5
62. Mannar D, Saville JW, Zhu X, Srivastava SS, Berezuk AM, Tuttle KS, Marquez AC, Sekirov I, Subramaniam S (2022) Science 375:760–764. https://doi.org/10.1126/science.abn7760
63. Jin Z, Du X, Xu Y, Deng Y, Liu M, Zhao Y, Zhang B, Li X, Zhang L, Peng C, Duan Y, Yu J, Wang L, Yang K, Liu F, Jiang R, Yang X, You T, Liu X, Yang X, Bai F, Liu H, Liu X, Guddat LW, Xu W, Xiao G, Qin C, Shi Z, Jiang H, Rao Z, Yang H (2020) Nature 582:289–293. https://doi.org/10.1038/s41586-020-2223-y
64. Osipiuk J, Jedrzejczak R, Tesar C, Endres M, Stols L, Babnigg G, Kim Y, Michalska K, Joachimiak A (2020) RSCB PDB 10. https://www.rcsb.org/structure/6w9c
65. Yin W, Mao C, Luan X, Shen D-D, Shen Q, Su H, Wang X, Zhou F, Zhao W, Gao M, Chang S, Xie Y-C, Tian G, Jiang H-W, Tao S-C, Shen J, Jiang Y, Jiang H, Xu Y, Zhang S, Zhang Y, Xu HE (2020) Science 368:1499–1504. https://doi.org/10.1126/science.abc1560
66. Kim Y, Wower J, Maltseva N, Chang C, Jedrzejczak R, Wilamowski M, Kang S, Nicolaescu V, Randall G, Michalska K, Joachimiak A (2021) Commun Biol 4:1–11. https://doi.org/10.1038/s42003-021-01735-9
67. Rosas-Lemus M, Minasov G, Shuvalova L, Inniss NL, Kiryukhina O, Brunzelle J, Satchell KJF (2020) Science Signaling 13:eabe1202. https://doi.org/10.1126/scisignal.abe1202
68. Fraser BJ, Beldar S, Seitova A, Hutchinson A, Mannar D, Li Y, Kwon D, Tan R, Wilson RP, Leopold K, Subramaniam S, Halabelian L, Arrowsmith CH, Bénard F (2022) Nat Chem Biol 18:963–971. https://doi.org/10.1038/s41589-022-01059-7

69. Biovia DS (2021) Dassault Systèmes, BIOVA Discovery Studio Visualizer 2021, v21.1.0.20298, San Diego: Dassault Systèmes (n.d.)
70. Gomez LM, Ferez FS, Calvet T, Bardia MF, Pons J (2020) Inorganica Chim Acta 506:119561–119561. https://doi.org/10.1016/j.ica.2020.119561
71. Bellamy LJ (1980) The Infrared Spectra of Complex Molecules, 2, 2nd edn. Chapman & Hall, London/New York
72. Nakamoto K (1997) Infrared and Raman Spectra of Inorganic and Coordination Compounds, 5th edn. John Wiley & Sons, New York
73. Zong G-C, Huo L-X, Ren N, Zhang J-J, Qi X-X, Gao J, Geng L-N, Wang S-P, Shi S-K (2015) Dalton Trans 44:14877–14886. https://doi.org/10.1039/C5DT01969A
74. Yang L, Powell DR, Houser RP (2007) Dalton Trans 9:955–964. https://doi.org/10.1039/B617136B
75. Ansari IA, Sama F, Raizada M, Shahid M, Ahmad M, Siddiqi ZA (2016) New J Chem 40:9840–9852. https://doi.org/10.1039/C6NJ02150F
76. Tarushi A, Totta X, Raptopoulou CP, Psycharis V, Psomasa G, Kessissoglou DP (2012) Dalton Trans 41:7082–7091. https://doi.org/10.1039/C2DT30547J
77. Chen BL, Ockwig NW, Millward AR, Contreras DS, Yaghi OM (2005) Angew. Chem. Int Ed 44:4745–4749. https://doi.org/10.1002/ange.200462787
78. Egli M, Sarkhel S (2007) Acc Chem Res 40:197–205. https://doi.org/10.1021/ar068174u
79. Xu F, Li G-M, Wang A-N, Han S-D, Pan J, Wang G-M (2021) Dalton Trans 50:18089–18096. https://doi.org/10.1039/D1DT02899E
80. Reimann CW, Block S, Perloff A (1966) Inorg Chem 5:1885–1889. https://doi.org/10.1021/ic50041a024
81. Espinosa E, Molins E (1998) Lacomte C. Chem Phys Lett 285:170–173. https://doi.org/10.1016/S0009-2614(98)00036-0
82. Hulswit RJG, de Haan CAM, Bosch BJ (2016) Chapter Two - Coronavirus Spike Protein and Tropism Changes. In: Ziebuhr J (ed) Advances in Virus Research. Academic Press, pp 29–57. https://doi.org/10.1016/bs.aivir.2016.08.004
83. Babaeekhou L, Ghane M, Abbas-Mohammadi M (2021) In silico targeting SARS-CoV-2 spike protein and main protease by biochemical compounds. Biologia (Bratisl) 76:3547–3565. https://doi.org/10.1007/s11756-021-00881-z
84. Cui W, Yang K, Yang H (2020) Front Mol Biosci 7:616341. https://www.frontiersin.org/articles/10.3389/fmolb.2020.616341
85. Haribabu J, Balakrishnan N, Swaminathan S, Peter J, Gayathri D, Echeverria C, Bhuvanesh N, Karvembu R (2021) Inorg Chem Commun 134:109029–109039. https://doi.org/10.1016/j.inoche.2021.109029

Publisher's Note Springer Nature remains neutral with regard to jurisdictional claims in published maps and institutional affiliations.

Springer Nature or its licensor (e.g. a society or other partner) holds exclusive rights to this article under a publishing agreement with the author(s) or other rightsholder(s); author self-archiving of the accepted manuscript version of this article is solely governed by the terms of such publishing agreement and applicable law.